Simultaneous Identification of Inverter and Machine Nonlinearities for Self-Commissioning of Electrical Synchronous Machine Drives

Simon Wiedemann and Christoph M. Hackl *Senior Member, IEEE*

***Abstract*—The proposed identification method allows for a simultaneous estimation of nonlinear output voltage deviations in voltage source inverters (VSIs) and nonlinear synchronous machine models. Based on the identified characteristics with the help of physically inspired structured artificial neural networks (ANNs), an efficient tuning of the current control system can be performed and the nonlinear voltage deviations caused by parasitic effects and dead-time distortions can be accurately compensated for. The identification is performed without position sensor while the rotor is mechanically locked by utilising measured phase currents and reference machine voltages only. Experiments for an interior permanent magnet synchronous machine (IPMSM) and a reluctance synchronous machine (RSM) show that the proposed method is capable of identifying the current dependent self-axis and cross-axis flux linkages, differential inductances and the nonlinear VSI voltage deviations as well as the phase resistance at the same time. The proposed method is fast and generic. Besides the rated machine current, voltage and frequency, no prior system knowledge is required making it applicable for the self-commissioning of any electrical synchronous machine drive.**

***Index Terms*—Identification, Self-Commissioning, Auto-tuning, Synchronous Machine, Inverter Dead-Time, Machine Characterisation, Flux Linkage Map, Machine Model, Artifical Neural Network, Encoderless.**

NOTATION

$\mathbb{N},\mathbb{R}$: natural, real numbers; $\boldsymbol{x} := (x_1,\ldots,x_n)^\top \in \mathbb{R}^{[}n]$: column vector, $n \in \mathbb{N}$ where "$^\top$" and ":=" mean "transposed" and "is defined as", resp.; $\boldsymbol{a}^\top\boldsymbol{b} := a_1b_1 + \cdots + a_nb_n$: scalar product of vectors $\boldsymbol{a}$, $\boldsymbol{b}$; $\|\boldsymbol{x}\| := \sqrt{\boldsymbol{x}^\top\boldsymbol{x}} = \sqrt{x_1^2+\cdots+x_n^2}$: Euclidean norm of $\boldsymbol{x}$; $\boldsymbol{X} \in \mathbb{R}^{n\times n}$: matrix ($n$ rows & columns); $\boldsymbol{X}^{-1}$: inverse of $\boldsymbol{X}$ (if exists). *Remark: All physical quantities are introduced and explained in the text.*

I. INTRODUCTION

Modern control methods and observer architectures of electrical machines rely mostly on accurate information of drive characteristics. Identified parameters of the linear machine model such as the phase resistances and inductances can be utilised to tune the current controllers [1]–[3] or observers and to compute the optimal reference currents for an energy efficient operation [2], [4]. This tuning can be further improved by the identification and utilisation of nonlinear flux linkage maps usually expressed in the synchronously rotating (d,q)-reference frame [2], [4]–[8] which allow to compute the differential inductances (in the following, the superscript d or q stands for the d- or q-axis, resp.). The automatic identification and tuning of the machine drive can be considered as self-commissioning/auto-tuning and is usually performed before machine operation via offline identification [1], [2], [9].

Self-commissioning algorithms heavily decrease the time required to characterise and tune an electrical machine drive compared to a manual process which, due to a lack of expertise and time of the control engineers, might lead to imprecise results and poor control dynamics [2] as well as an energy inefficient operation [9]. The importance of an automatic commissioning becomes obvious if one considers that around $53\,\%$ of the globally generated energy is consumed by electrical machines [10]. Despite several improvements on energy efficient control methods in the last 30 years [4], only little effort seems to be taken for a rigorous adoption of these technologies within the industry. A comprehensive review on parameter identification and self-commissioning of ac drives can be found in [1].

Furthermore, not only control architectures but also identification algorithms are prone to perform inaccurately if inverter nonlinear effects expressed through output voltage errors of the voltage source inverter are not accurately compensated for [11]–[13]. Therefore, the characterisation of these VSI voltage errors must be (and usually is) performed before (and separately from) the machine identification process. Moreover, the state of the art voltage error identification methods [11], [12] rely on already tuned current controllers which requires knowledge and, therefore, leads to an iterative and repetitive commissioning process which is still not most efficient.

Magnetic saturation is usually modelled either by the stator flux linkage maps $\psi_s^d(i_s^d,i_s^q)$ and $\psi_s^q(i_s^d,i_s^q)$ depended on the stator d and q currents or vise versa, i.e. $i_s^d(\psi_s^q,\psi_s^q)$ and $i_s^q(\psi_s^q,\psi_s^q)$. The former is usually more complex to model with e.g. neural networks [5], [14], [15], piece-wise nonlinear functions [16], or nonlinear models [17], [18]. The latter can be expressed by polynomials [18]–[20] making it simpler to be identified. Typically, three offline identification methods can be applied to estimate the saturation characteristics:

Simon Wiedemann is with the Research and Development Department at MACCON GmbH, Aschauer Str. 21, Munich 81549, Germany (e-mail: s.wiedemann@maccon.de).

Christoph M. Hackl is with the Institute for Sustainable Energy Systems (ISES), Hochschule München (HM) University of Applied Sciences, Munich 80335, Germany (e-mail: christoph.hackl@hm.edu).

This work was supported by the Federal Ministry for "Economic Affairs and Climate Action" (19I21030H - KIRA).

Constant speed methods (CSM) [6], [19]–[21] are most accurate but require much time and extensive measurement equipment including a load machine and take rather longer. Dynamic testing methods (DTM) [6], [22] perform the characterisation faster compared to CSM and need less equipment such as a load machine but are limited in the range of characterisation currents due to very fast rotor accelerations during the identification. Standstill methods (SSM) [15], [16], [23], [24] allow for the fastest characterisation within a few seconds or less. However, estimation results may be negatively affected if the rotor starts to move from the rest point due to non-negligible torques produced by the injected currents. In this case, the rotor needs to be locked mechanically. Moreover, for the aforementioned SSMs, the flux linkage maps are estimated by an open loop integrator which may lead to a drift in the estimation results due to measurement inaccuracies and/or noise. For all of the methods above, an identification error exists due to voltage deviations arising from uncompensated VSI nonlinearities or uncertainties in the stator resistance. However, it depends on the severity of both effects if one needs to implement a compensation or not [9]. In particular, SSMs seem to be more robust in this regard [24]. For industrial drives (as experience indicates), it is always beneficial if not even necessary to identify and compensate for VSI nonlinearities to improve the identification results.

Contributions of this paper are: (C1) A simple and very fast offline standstill identification method which can be performed position sensorless (encoderless) where the machine under test (MUT) is excited by low frequency voltage signals resulting in phase current responses in d- or q-axis direction; and (C2) An effective post-processing nonlinear least-squares algorithm which utilises the measured currents and the stator reference voltages only for the simultaneous identification of VSI voltage error characteristics *and* nonlinear synchronous machine models considering self-axis *and* cross-axis flux linkages *and* all differential inductances as well as the stator resistance. VSI voltage error and flux linkages are approximated by structured ANNs which exploit intrinsic physical properties of the approximated quantities. The proposed method has the following advantages compared to state-of-the-art machine identification methods: (A1) The a priori compensation of VSI nonlinearities is *not* required in contrast to CSM, DTM and SSM; (A2) the phase resistance does *not* need to be known a priori in contrast to SSM; (A3) *no* current controllers are needed in contrast to CSM and DTM; (A4) *no* load machine (in contrast to CSM) or flywheel (in contrast to DTM) is necessary; (A5) the identification is performed as fast as with SSM and, therefore, is much faster than for CSM and DTM; (A6) the phase resistance is identified at the same time which is not the case for CSM, DTM and SSM; and (A7) compared to the competitive SSM, no open loop integration effects can occur, which makes this method more robust to measurement inaccuracies and/or noise. Furthermore, the proposed method has the following advantages compared to state-of-the-art VSI identification methods (see e.g. [11], [12]): (A8) the machine phase resistance and equivalent VSI resistance do not have to be known a priori; (A9) no current controllers and special current reference signals are necessary; and (A10) the identification is performed much faster which leads to a significantly reduced machine heating (a general disadvantage of most available methods). Nevertheless, it is recommended that the rotor is locked during the identification of the proposed method (at least for a q-axis characterisation) which can be seen as a drawback of the proposed method.

The remainder of the paper is organized as follows: Section II introduces the VSI voltage deviations and its implication on drive performance and introduces a modelling technique suitable for compensation and identification. Section III shows how the current dynamics are modelled (in general and at standstill) while nonlinear magnetic effects (such as saturation) of synchronous machines are considered. Section IV describes the overall identification process including system excitation, post-processing and how the electric drive characteristics are identified simultaneously. Finally, Section V validates the proposed identification and modelling techniques via measurements for an IPMSM and a RSM. Section VI concludes the paper.

II. Voltage Source Inverter Nonlinearities

Besides their modulated approximation of sinusoidal voltages, VSIs induce additional errors in their produced output voltages which result in deviations compared to the desired phase reference voltage $u^p_{\mathrm{s,ref}} \in \{u^a_{\mathrm{s,ref}}, u^b_{\mathrm{s,ref}}, u^c_{\mathrm{s,ref}}\}$ obtained from the control system. These deviations in the actually applied phase voltage $u^p_{\mathrm{s}} \in \{u^a_{\mathrm{s}}, u^b_{\mathrm{s}}, u^c_{\mathrm{s}}\}$ to the electrical machine will lead to (a) performance deterioration of the current controllers and/or outer control loops, (b) harmonics in the machine, torque and currents and (c) deteriorated estimation results for observers or identification architectures. The reasons for voltage deviations are mainly: voltage transients of the power semiconductors (diodes and transistors) [9], [13], dead-times between consecutive switching events [25], zero current clamping effects [26] and nonlinear voltage drops over the semiconductors through on-state and resistive voltages [13], [27]. Furthermore, the voltage deviations nonlinearly depend on several system signals and parasitic effects such as the: DC-link voltage u_{dc}, switching frequency $f_{\mathrm{sw}} = 1/T_{\mathrm{sw}}$ of the power transistors, stator phase current $i^p_{\mathrm{s}} \in \{i^a_{\mathrm{s}}, i^b_{\mathrm{s}}, i^c_{\mathrm{s}}\}$ and its respective sign $\mathrm{sign}(i^p_{\mathrm{s}})$ [13], [25], VSI output capacitance C_{out} [9], [13], temperature and ageing effects [28].

A. Modeling of voltage deviations due to VSI nonlinearities

The typical phase voltage deviations Δu^p_{s} of some phase $p \in \{a, b, c\}$ are illustrated in Fig. 1. Two main regions can be distinguished. In the high-current region, Δu^p_{s} becomes approximately a constant whereas a distinctive current dependency in the shape of a sigmoid function is present in the low-current region. In the high-current region, the magnitude of the voltage deviation can be computed as [25], [29]

$$M_{\Delta u_{\mathrm{s}}} = \Big[(u_{\mathrm{dc}} - u_{\mathrm{sat}} + u_{d_{\mathrm{on}}})\tfrac{T_{\mathrm{d}}+T_{\mathrm{on}}-T_{\mathrm{off}}}{T_{\mathrm{sw}}} + \tfrac{u_{\mathrm{sat}}+u_{d_{\mathrm{on}}}}{2} + \tfrac{(u_{\mathrm{sat}}-u_{d_{\mathrm{on}}})u^p_{\mathrm{s,ref}}}{u_{\mathrm{dc}}}\Big], \tag{1}$$

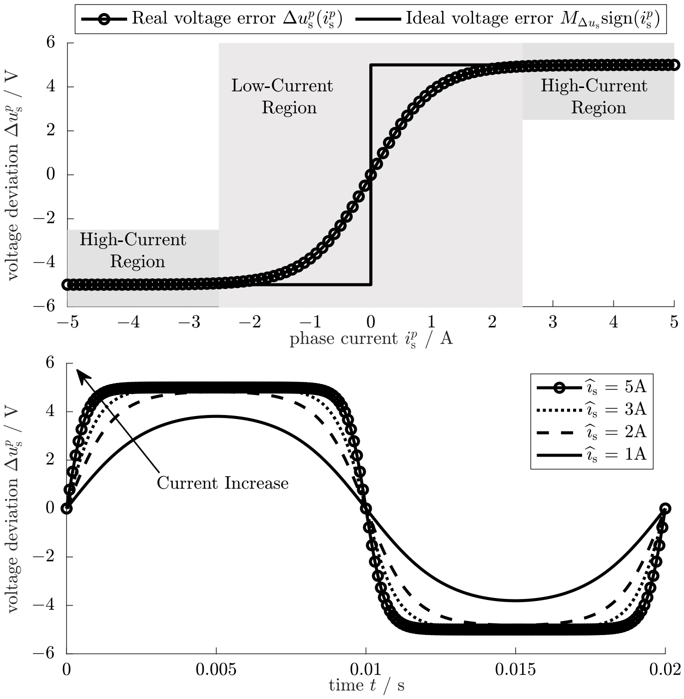

Figure 1: Ideal vs. real voltage deviation over i_s^p (top); real voltage deviation $\Delta u_s^p(i_s^p)$ over one period of a sinusoidal phase current i_s^p with different amplitudes $\widehat{\imath}_s$ (bottom).

which depends on dc-link voltage u_{dc}, transistor threshold voltage u_{sat} and diode threshold voltage $u_{d_{on}}$ and phase reference voltage $u_{s,ref}^p$, dead time T_d and switching period T_{sw} where on and off times are defined as

$$T_{on} = T_{d_{on}} + \tfrac{T_{f_{min}}}{2} \qquad \text{and} \qquad T_{off} = T_{d_{off}} + \tfrac{T_{r_{min}}}{2}, \qquad (2)$$

i.e. the times of the negative and positive voltage areas as a result of the on and off delay times $T_{d_{on}}$ and $T_{d_{off}}$ and the minimal rise and fall times $T_{r_{min}}$ and $T_{f_{min}}$, respectively.

The voltage error model becomes more accurate if one considers that T_{off} in (2) is a nonlinear function

$$T_{off} = f(C_{out}, u_{dc}, i_s^p, T_{d_{off}}, T_{r_{min,max}}, T_{f_{min}}), \qquad (3)$$

where C_{out} is a composition of different equivalent VSI leg capacitors and the output capacitance of the half bridge (for details see [9], [13]). In conclusion, the voltage deviation Δu_s^p due to the VSI nonlinearities affects each phase voltage, i.e.

$$\forall\, p \in \{a, b, c\}: \qquad u_s^p = u_{s,ref}^p - \Delta u_s^p(M_{\Delta u_s}, i_s^p, \dots). \quad (4)$$

Remark 1. *Due to the switching nature of the VSI, all voltages in* (4) *actually represent averaged voltages over one switching period* T_{sw}, *i.e.,* $\overline{u}(t) := \int_{t-T_{sw}}^{t} u(\tau)\,d\tau$.

B. ANN-based approximation of VSI voltage deviations

For self-commissioning, an accurate representation of Δu_s^p is required within the control system in order to compensate for the VSI nonlinearities. Using a physical model composed of (1), (2), (3) and (4) is crucial for the understanding of the error source but impractical for a real-time compensation and implementation as most parameters and quantities in (1), (2), (3) and (4) are neither (exactly) known nor measured.

1) Approximation in (a, b, c)*-reference frame:* Therefore, a simple feed-forward artificial neural network (ANN) as shown in Fig. 2 is proposed. This allows to model $\Delta u_s^p = f_{ann}^{vsi}(i_s^p, u_{dc}, T_{sw}, \dots)$ as a nonlinear function of one or more inputs. This makes it very flexible, accurate and efficient in representing experimental data analytically within a digital environment utilising a minimum amount of model parameters and system storage compared to look-up tables (LUTs) [11] or trapezoidal models [30]. Recalling Fig. 1 reveals that one input – the phase current i_s^p – is sufficient. Therefore,

$$\forall p \in \{a, b, c\}: \quad \Delta u_s^p \approx \Delta\widehat{u}_s^p(i_s^p) := f_{ann}^{vsi}(i_s^p) \qquad (5)$$

is chosen as approximation $\Delta\widehat{u}_s^p(i_s^p)$ of each phase VSI nonlinearity for self-commissioning (assuming a constant dc-link voltage). The proposed ANN architecture is illustrated in Fig. 2 and consists of one input layer (Layer 0) and one output layer (Layer 2) each with identity activation function $\Phi_0(y) = \Phi_2(y) = \Phi_{id}(y) = y$ (cf. [31]) and one hidden layer (Layer 1) with two neurons utilizing the soft-sign activation function $\Phi_{1,1}(y) = \Phi_{1,2}(y) = \Phi_{SoSi}(y) = \frac{y}{1+|y|}$ (cf. [32]).

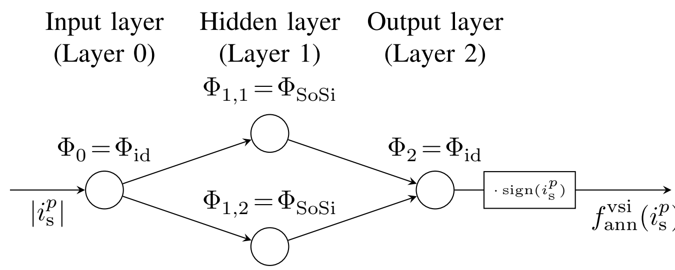

Figure 2: ANN for approximation of VSI voltage deviation Δu_s^p of phase $p \in \{a, b, c\}$ by $\Delta\widehat{u}_s^p := f_{ann}^{vsi}(i_s^p)$.

With the ANN architecture as in Fig. 2, the VSI voltage deviation Δu_s^p of phase $p \in \{a, b, c\}$ will be approximated by

$$\Delta\widehat{u}_s^p(i_s^p) := f_{ann}^{vsi}(i_s^p) = \left(\frac{w_{2,1}^{vsi}\left(w_{1,1}^{vsi}|i_s^p| + b_{1,1}^{vsi}\right)}{1+\left|w_{1,1}^{vsi}|i_s^p| + b_{1,1}^{vsi}\right|} + \frac{w_{2,2}^{vsi}\left(w_{1,2}^{vsi}|i_s^p| + b_{1,2}^{vsi}\right)}{1+\left|w_{1,2}^{vsi}|i_s^p| + b_{1,2}^{vsi}\right|} \right) \mathrm{sign}(i_s^p) \quad (6)$$

with overall six ANN parameters[1], i.e. $\boldsymbol{w}_1^{vsi} := (w_{1,1}^{vsi}, w_{1,2}^{vsi})^\top$, $\boldsymbol{b}_1^{vsi} := (b_{1,1}^{vsi}, b_{1,2}^{vsi})^\top$ of Layer 1 and $\boldsymbol{w}_2^{vsi} := (w_{2,1}^{vsi}, w_{2,2}^{vsi})^\top$ of Layer 2 which need to be identified.

Remark 2 (ANN-training for one phase)**.** *It is sufficient to train the ANN as in* (6) *for the VSI voltage deviation* $\Delta u_s^p(i_s^p)$ *for one phase only (e.g.,* $p = a$*). For real-time compensation, it must be implemented for each phase* $p \in \{a, b, c\}$ *separately and fed by the respective phase current* i_s^p.

Remark 3 (Dependency on dc-link voltage)**.** *In general, the VSI nonlinearity may also depend on the dc-link voltage* u_{dc}*. To consider a varying* u_{dc}*, the ANN structure in* (6) *has to be extended by replacing the terms* $x_1 := w_{1,1}^{vsi}|i_s^p| + b_{1,1}^{vsi}$ *and* $x_2 := w_{1,2}^{vsi}|i_s^p| + b_{1,2}^{vsi}$ *by* $x_1 := w_{1,1}^{vsi}|i_s^p| + w_{1,3}^{vsi}u_{dc} + b_{1,1}^{vsi}$ *and*

[1] Explanation of ANN notation (cf. [31]): Weight $w_{i,j}^z$ and bias $b_{i,j}^z$ are identified by their subscripts i and j indicating layer and neuron, respectively, and by their superscript z indicating the system to be estimated by the ANN.

$x_2 := w^{\rm vsi}_{1,2}|i^p_{\rm s}| + w^{\rm vsi}_{1,4}u_{\rm dc} + b^{\rm vsi}_{1,2}$, respectively. Then, the VSI-ANN depends not only on the phase current $i^p_{\rm s}$ but also on the dc-link voltage $u_{\rm dc}$ and has two more weights $w^{\rm vsi}_{1,3}$ and $w^{\rm vsi}_{1,4}$.

2) Approximation in (d, q)-reference frame (required for later ANN training): In the (d, q)-reference frame, the VSI voltage deviations for $\phi_{\rm p} = 0^\circ$ (standstill[2]) become

$$\Delta \boldsymbol{u}^{dq}_{\rm s}(\boldsymbol{i}^{dq}_{\rm s}) := \begin{pmatrix} \Delta u^d_{\rm s}(\boldsymbol{i}^{dq}_{\rm s}) \\ \Delta u^q_{\rm s}(\boldsymbol{i}^{dq}_{\rm s}) \end{pmatrix} = \boldsymbol{T}_{\rm c} \begin{pmatrix} \Delta u^a_{\rm s}(i^a_{\rm s}) \\ \Delta u^b_{\rm s}(i^b_{\rm s}) \\ \Delta u^c_{\rm s}(i^c_{\rm s}) \end{pmatrix} \tag{7}$$

with Clarke transformation matrix [33, Chap. 14]

$$\boldsymbol{T}_{\rm c} := \kappa \begin{bmatrix} 1 & -\frac{1}{2} & -\frac{1}{2} \\ 0 & \frac{\sqrt{3}}{2} & -\frac{\sqrt{3}}{2} \end{bmatrix} \Leftrightarrow \boldsymbol{T}_{\rm c}^{-1} := \frac{1}{\kappa} \begin{bmatrix} \frac{2}{3} & 0 \\ -\frac{1}{3} & \frac{\sqrt{3}}{3} \\ -\frac{1}{3} & -\frac{\sqrt{3}}{3} \end{bmatrix}$$

where $\kappa \in \{2/3; \sqrt{2/3}\}$ allows for an amplitude or power invariant transformation, respectively. In view of

$$\begin{pmatrix} i^a_{\rm s} \\ i^b_{\rm s} \\ i^c_{\rm s} \end{pmatrix} = \boldsymbol{T}_{\rm c}^{-1} \boldsymbol{i}^{dq}_{\rm s} = \begin{pmatrix} -\frac{1}{3\kappa} i^d_{\rm s} + \frac{\sqrt{3}}{3\kappa} i^q_{\rm s} \\ -\frac{1}{3\kappa} i^d_{\rm s} + \frac{\sqrt{3}}{3\kappa} i^q_{\rm s} \\ -\frac{1}{3\kappa} i^d_{\rm s} - \frac{\sqrt{3}}{3\kappa} i^q_{\rm s} \end{pmatrix},$$

the transformation (7) is also applicable for the approximation $\Delta \widehat{u}^p_{\rm s}(i^p_{\rm s}) \approx f^{\rm vsi}_{\rm ann}(i^p_{\rm s})$ for all $p \in \{a, b, c\}$ as in (6) resulting in

$$\Delta \boldsymbol{u}^{dq}_{\rm s}(\boldsymbol{i}^{dq}_{\rm s}) \approx \Delta \widehat{\boldsymbol{u}}^{dq}_{\rm s}(\boldsymbol{i}^{dq}_{\rm s}) := \begin{pmatrix} \Delta \widehat{u}^d_{\rm s}(\boldsymbol{i}^{dq}_{\rm s}) \\ \Delta \widehat{u}^q_{\rm s}(\boldsymbol{i}^{dq}_{\rm s}) \end{pmatrix}$$
$$= \kappa \begin{pmatrix} f^{\rm vsi}_{\rm ann}(\frac{2}{3\kappa} i^d_{\rm s}) - \frac{1}{2} f^{\rm vsi}_{\rm ann}(-\frac{1}{3\kappa} i^d_{\rm s} + \frac{\sqrt{3}}{3\kappa} i^q_{\rm s}) - \frac{1}{2} f^{\rm vsi}_{\rm ann}(-\frac{1}{3\kappa} i^d_{\rm s} - \frac{\sqrt{3}}{3\kappa} i^q_{\rm s}) \\ \frac{\sqrt{3}}{2} f^{\rm vsi}_{\rm ann}(-\frac{1}{3\kappa} i^d_{\rm s} + \frac{\sqrt{3}}{3\kappa} i^q_{\rm s}) - \frac{\sqrt{3}}{2} f^{\rm vsi}_{\rm ann}(-\frac{1}{3\kappa} i^d_{\rm s} - \frac{\sqrt{3}}{3\kappa} i^q_{\rm s}) \end{pmatrix}, \tag{8}$$

which implies that the VSI-ANN not only depends on one current in the (d, q)-reference frame but may depend on both.

III. Synchronous Machine Nonlinearities

The electrical dynamics of a synchronous machine in the (d, q)-reference frame are given by [20], [33]

$$\boldsymbol{u}^{dq}_{\rm s} = R_{\rm s} \boldsymbol{i}^{dq}_{\rm s} + \tfrac{\rm d}{{\rm d}t} \boldsymbol{\psi}^{dq}_{\rm s}(\boldsymbol{i}^{dq}_{\rm s}) + \omega_{\rm p} \boldsymbol{J} \boldsymbol{\psi}^{dq}_{\rm s}(\boldsymbol{i}^{dq}_{\rm s}), \tag{9}$$

with stator voltages $\boldsymbol{u}^{dq}_{\rm s} = (u^d_{\rm s}, u^q_{\rm s})^\top$, stator (phase) resistance $R_{\rm s}$, stator currents $\boldsymbol{i}^{dq}_{\rm s} = (i^d_{\rm s}, i^q_{\rm s})^\top$, electrical synchonous angular velocty $\omega_{\rm p} = \frac{\rm d}{{\rm d}t}\phi_{\rm p}$ (where $\omega_{\rm p} = n_{\rm p}\omega_{\rm m}$ with pole pair number $n_{\rm p}$ and mechanical angular velocity $\omega_{\rm m}$), flux linkages $\boldsymbol{\psi}^{dq}_{\rm s}(\boldsymbol{i}^{dq}_{\rm s}) = (\psi^d_{\rm s}(i^d_{\rm s}, i^q_{\rm s}), \psi^q_{\rm s}(i^d_{\rm s}, i^q_{\rm s}))^\top$ and rotation matrix $\boldsymbol{J} := \begin{bmatrix} 0 & -1 \\ 1 & 0 \end{bmatrix}$. The time derivative of the flux linkages

$$\tfrac{\rm d}{{\rm d}t} \boldsymbol{\psi}^{dq}_{\rm s}(\boldsymbol{i}^{dq}_{\rm s}) = \underbrace{\begin{bmatrix} \overbrace{\frac{\partial \psi^d_{\rm s}(i^d_{\rm s}, i^q_{\rm s})}{\partial i^d_{\rm s}}}^{=:L^{dd}_{\rm s}(i^d_{\rm s}, i^q_{\rm s})} & \overbrace{\frac{\partial \psi^d_{\rm s}(i^d_{\rm s}, i^q_{\rm s})}{\partial i^q_{\rm s}}}^{=:L^{dq}_{\rm s}(i^d_{\rm s}, i^q_{\rm s})} \\ \underbrace{\frac{\partial \psi^q_{\rm s}(i^d_{\rm s}, i^q_{\rm s})}{\partial i^d_{\rm s}}}_{=:L^{qd}_{\rm s}(i^d_{\rm s}, i^q_{\rm s})} & \underbrace{\frac{\partial \psi^q_{\rm s}(i^d_{\rm s}, i^q_{\rm s})}{\partial i^q_{\rm s}}}_{:=L^{qq}_{\rm s}(i^d_{\rm s}, i^q_{\rm s})} \end{bmatrix}}_{=:\boldsymbol{L}^{dq}_{\rm s}(\boldsymbol{i}^{dq}_{\rm s}) \in \mathbb{R}^{2\times 2}} \underbrace{\begin{pmatrix} \frac{\rm d}{{\rm d}t} i^d_{\rm s} \\ \frac{\rm d}{{\rm d}t} i^q_{\rm s} \end{pmatrix}}_{=:\frac{\rm d}{{\rm d}t}\boldsymbol{i}^{dq}_{\rm s}} \tag{10}$$

gives the current dynamics with differential inductance matrix $\boldsymbol{L}^{dq}_{\rm s}(\boldsymbol{i}^{dq}_{\rm s})$ which consists of the differential inductances $L^{dd}_{\rm s}(i^d_{\rm s}, i^q_{\rm s})$ and $L^{qq}_{\rm s}(i^d_{\rm s}, i^q_{\rm s})$ and the differential mutual (cross-coupling) inductance $L^{dq}_{\rm s}(i^d_{\rm s}, i^q_{\rm s}) = L^{qd}_{\rm s}(i^d_{\rm s}, i^q_{\rm s})$. For anisotropic machines which exhibit saturation effects such as the interior permanent magnet machine (IPMSM) or the reluctance synchronous machine (RSM), all differential inductances depend on both currents $\boldsymbol{i}^{dq}_{\rm s} = (i^d_{\rm s}, i^q_{\rm s})^\top$. For anisotropic machines with purely self-saturation effects, the inductances simplify to $L^{dd}_{\rm s}(i^d_{\rm s})$, $L^{qq}_{\rm s}(i^q_{\rm s})$ (both only depend on their respective axis current) and $L^{dq}_{\rm s}(i^d_{\rm s}, i^q_{\rm s}) = L^{qd}_{\rm s}(i^d_{\rm s}, i^q_{\rm s}) = 0$.

[2]The Park transformation for $\phi_{\rm p} = 0^\circ$ simplifies to a unity matrix.

A. Simplified current dynamics at standstill

In this work, the MUT is identified at standstill (i.e. $\omega_{\rm p} = 0\frac{\rm rad}{\rm s}$) such that (9) reduces to

$$\boldsymbol{u}^{dq}_{\rm s} = R_{\rm s} \boldsymbol{i}^{dq}_{\rm s} + \tfrac{\rm d}{{\rm d}t} \boldsymbol{\psi}^{dq}_{\rm s}(\boldsymbol{i}^{dq}_{\rm s}) \tag{11}$$

which leads to the simplified current dynamics at standstill

$$\tfrac{\rm d}{{\rm d}t} \boldsymbol{i}^{dq}_{\rm s} = \boldsymbol{L}^{dq}_{\rm s}(\boldsymbol{i}^{dq}_{\rm s})^{-1} \big(\boldsymbol{u}^{dq}_{\rm s} - R_{\rm s} \boldsymbol{i}^{dq}_{\rm s}\big). \tag{12}$$

Invoking forward Euler discretization (i.e. $\frac{\rm d}{{\rm d}t}x \approx \frac{x[n+1]-x[n]}{T_{\rm s}}$ with sampling time $T_{\rm s}$ and instants n and $n+1$) yields

$$\boldsymbol{i}^{dq}_{\rm s}[n+1] \approx T_{\rm s} \boldsymbol{L}^{dq}_{\rm s}(\boldsymbol{i}^{dq}_{\rm s}[n])^{-1} \big(\boldsymbol{u}^{dq}_{\rm s}[n] - R_{\rm s} \boldsymbol{i}^{dq}_{\rm s}[n]\big) + \boldsymbol{i}^{dq}_{\rm s}[n],$$

which may be rewritten in a more compact form as follows

$$\boldsymbol{i}^{dq}_{\rm s}[n+1] \approx \underbrace{\big[\boldsymbol{I}_2 - R_{\rm s} T_{\rm s} \boldsymbol{L}^{dq}_{\rm s}(\boldsymbol{i}^{dq}_{\rm s}[n])^{-1}\big]}_{=:\boldsymbol{A}^{dq}_{\rm s}[n] \in \mathbb{R}^{2\times 2}} \boldsymbol{i}^{dq}_{\rm s}[n] + \underbrace{T_{\rm s} \boldsymbol{L}^{dq}_{\rm s}(\boldsymbol{i}^{dq}_{\rm s}[n])^{-1}}_{=:\boldsymbol{B}^{dq}_{\rm s}[n] \in \mathbb{R}^{2\times 2}} \boldsymbol{u}^{dq}_{\rm s}[n]. \tag{13}$$

If the cross-coupling effects (i.e. assuming $L^{dq}_{\rm s} = L^{qd}_{\rm s} = 0$) are neglected and only the self-axis differential inductances (i.e. $L^{dd}_{\rm s}(i^d_{\rm s}, 0)$ and $L^{qq}_{\rm s}(0, i^q_{\rm s})$) are considered, one obtains the simplified difference equations

$$i^d_{\rm s}[n+1] \approx \underbrace{\Big(1 - \frac{T_{\rm s} R_{\rm s}}{L^{dd}_{\rm s}(i^d_{\rm s}[n], 0)}\Big)}_{=:a^d_{\rm s}[n]} i^d_{\rm s}[n] + \underbrace{\frac{T_{\rm s}}{L^{dd}_{\rm s}(i^d_{\rm s}[n], 0)}}_{=:b^d_{\rm s}[n]} u^d_{\rm s}[n] \tag{14}$$

for the d-axis current and

$$i^q_{\rm s}[n+1] \approx \underbrace{\Big(1 - \frac{T_{\rm s} R_{\rm s}}{L^{qq}_{\rm s}(0, i^q_{\rm s}[n])}\Big)}_{=:a^q_{\rm s}[n]} i^q_{\rm s}[n] + \underbrace{\frac{T_{\rm s}}{L^{qq}_{\rm s}(0, i^q_{\rm s}[n])}}_{=:b^q_{\rm s}[n]} u^q_{\rm s}[n] \tag{15}$$

for the q-axis current, respectively.

B. ANN-based approximation of self-axis flux linkages

The flux linkages can be written as [34]

$$\boldsymbol{\psi}^{dq}_{\rm s}(\boldsymbol{i}^{dq}_{\rm s}) = \begin{pmatrix} \psi^d_{\rm s,self}(i^d_{\rm s}) \\ \psi^q_{\rm s,self}(i^q_{\rm s}) \end{pmatrix} + \begin{pmatrix} \psi^d_{\rm s,cross}(i^d_{\rm s}, i^q_{\rm s}) \\ \psi^q_{\rm s,cross}(i^d_{\rm s}, i^q_{\rm s}) \end{pmatrix} \tag{16}$$

where $\psi^d_{\rm s,self}(i^d_{\rm s})$ and $\psi^q_{\rm s,self}(i^q_{\rm s})$ reflect the self-axis flux linkages which only depend on the respective axis currents, whereas $\psi^d_{\rm s,cross}(i^d_{\rm s}, i^q_{\rm s})$ and $\psi^q_{\rm s,cross}(i^d_{\rm s}, i^q_{\rm s})$ describe the cross-coupling flux linkages which depend on both currents. For the initial self-axis identification, the cross-coupling effects are neglected and, therefore, for each axis $x \in \{d, q\}$,

$$\psi^x_{\mathrm{s,self}}(i^x_{\mathrm{s}}) \approx \widehat{\psi}^x_{\mathrm{s,self}}(i^x_{\mathrm{s}}) := f_{\mathrm{ann}}^{\psi^x_{\mathrm{s,self}}}(i^x_{\mathrm{s}}) \tag{17}$$

is chosen as approximation $\widehat{\psi}^x_{\mathrm{s,self}}(i^x_{\mathrm{s}})$ of the self-axis flux linkages $\psi^x_{\mathrm{s,self}}(i^x_{\mathrm{s}})$. For each axis $x \in \{d, q\}$, each proposed ANN architecture has one input and one output as illustrated in Fig. 3 and consists of one input layer (Layer 0) and one output layer (Layer 2) each with identity activation function $\Phi_0(y) = \Phi_2(y) = \Phi_{\mathrm{id}}(y) = y$ and one hidden layer (Layer 1) with two neurons utilizing the $\tanh$ activation function $\Phi_{1,1}(y) = \Phi_{1,2}(y) = \Phi_{\tanh}(y) = \frac{1-e^{-2y}}{1+e^{-2y}}$ (cf. [31]).

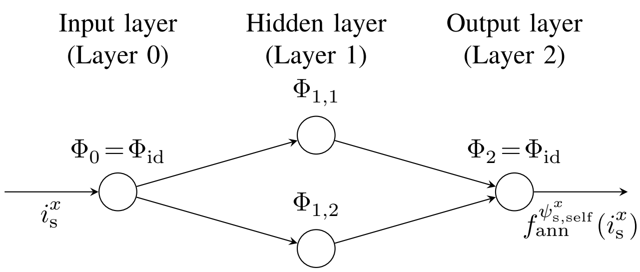

Figure 3: ANN for approximation of self-axis flux linkage $\psi^x_{\mathrm{s,self}}(i^x_{\mathrm{s}})$ of axis $x \in \{d, q\}$ by $\widehat{\psi}^x_{\mathrm{s,self}}(i^x_{\mathrm{s}}) := f_{\mathrm{ann}}^{\psi^x_{\mathrm{s,self}}}(i^x_{\mathrm{s}})$.

For the ANN as in Fig. 3 and $x \in \{d, q\}$, each self-axis flux linkage is approximated by

$$\begin{aligned}\widehat{\psi}^x_{\mathrm{s,self}}(i^x_{\mathrm{s}}) = {} & w^{x,\mathrm{self}}_{2,1} \frac{1-\exp\left(-2(w^{x,\mathrm{self}}_{1,1} i^x_{\mathrm{s}} + b^{x,\mathrm{self}}_{1,1})\right)}{1+\exp\left(-2(w^{x,\mathrm{self}}_{1,1} i^x_{\mathrm{s}} + b^{x,\mathrm{self}}_{1,1})\right)} \\ & + w^{x,\mathrm{self}}_{2,2} \frac{1-\exp\left(-2(w^{x,\mathrm{self}}_{1,2} i^x_{\mathrm{s}} + b^{x,\mathrm{self}}_{1,2})\right)}{1+\exp\left(-2(w^{x,\mathrm{self}}_{1,2} i^x_{\mathrm{s}} + b^{x,\mathrm{self}}_{1,2})\right)} + b^{x,\mathrm{self}}_2\end{aligned} \tag{18}$$

with (six or) seven ANN parameters $\boldsymbol{w}^{x,\mathrm{self}}_1 := (w^{x,\mathrm{self}}_{1,1}, w^{x,\mathrm{self}}_{1,2})^\top$, $\boldsymbol{b}^{x,\mathrm{self}}_1 := (b^{x,\mathrm{self}}_{1,1}, b^{x,\mathrm{self}}_{1,2})^\top$ of Layer 1 and $\boldsymbol{w}^{x,\mathrm{self}}_2 := (w^{x,\mathrm{self}}_{2,1}, w^{x,\mathrm{self}}_{2,2})^\top$ and $b^{x,\mathrm{self}}_2$ of Layer 2 which need to be identified per axis.

If the considered (I)PMSM is rather linear, one can also use

$$\widehat{\psi}^x_{\mathrm{s,self}}(i^x_{\mathrm{s}}) := w^{x,\mathrm{self}}_{2,1} i^x_{\mathrm{s}} - w^{x,\mathrm{self}}_{2,2} \ln\big(1 + \exp(-i^x_{\mathrm{s}})\big) + b^{x,\mathrm{self}}_2 \tag{19}$$

with $\Phi_{1,1}(y) = y$ (identity) and $\Phi_{1,2}(y) = \Phi_{\mathrm{spa}}(y) := \ln(1 + e^y)$ [soft-plus activation (spa) function [35]] which, in Layer 2, are weighted by $w^{x,\mathrm{self}}_{2,1}$ describing the linear property and $w^{x,\mathrm{self}}_{2,2}$ accounting for the saturation characteristic. In (18) and (19), the permanent magnet flux linkage is considered by the bias $b^{x,\mathrm{self}}_2$ for both axis $x \in \{d, q\}$, respectively.

Remark 4. *Please note that, (i) for RSMs without permanent magnet, the biases $b^{d,\mathrm{self}}_2 = b^{q,\mathrm{self}}_2 = 0$ can be neglected; whereas (ii) for IPMSMs, $b^{q,\mathrm{self}}_2 = 0$ and $b^{d,\mathrm{self}}_2 = \psi_{\mathrm{pm}}(\vartheta_{\mathrm{r}}) > 0$, or (iii) for permanent-magnet assisted RSMs (PMA-RSMs) [36], $b^{d,\mathrm{self}}_2 = 0$ and $b^{q,\mathrm{self}}_2 = \psi_{\mathrm{pm}}(\vartheta_{\mathrm{r}}) < 0$ must be introduced to model the (rotor) temperature-dependent flux linkage of the permanent magnet. It is usually identified while the machine rotates (see [5]–[7]), but it can also be identified at standstill [8]. A priori knowledge, e.g., in form of a look-up table (LUT), can be exploited to reduce identification effort.*

Remark 5. *If apparent inductances $L^{xx}_{\mathrm{s,app}}$ are required those can easily be computed with the help of the flux linkage ANNs as follows $L^{xx}_{\mathrm{s,app}} = \frac{f_{\mathrm{ann}}^{\psi^x_{\mathrm{s,self}}}(i^x_{\mathrm{s}})}{i^x_{\mathrm{s}}}$ for $x \in \{d, q\}$.*

C. ANN-based approximation of cross-axis flux linkages

For the cross-axis identification, for each axis $x \in \{d, q\}$,

$$\psi^x_{\mathrm{s,cross}}(i^d_{\mathrm{s}}, i^q_{\mathrm{s}}) \approx \widehat{\psi}^x_{\mathrm{s,cross}}(i^d_{\mathrm{s}}, i^q_{\mathrm{s}}) := f_{\mathrm{ann}}^{\psi^x_{\mathrm{s,cross}}}(i^d_{\mathrm{s}}, i^q_{\mathrm{s}}) \tag{20}$$

is chosen as the approximation $\widehat{\psi}^x_{\mathrm{s,cross}}(i^d_{\mathrm{s}}, i^q_{\mathrm{s}})$ of the cross-axis flux linkages $\psi^x_{\mathrm{s,cross}}(i^d_{\mathrm{s}}, i^q_{\mathrm{s}})$ in (16). The proposed ANN architecture for cross-axis identification is shown in Fig. 4. It has two inputs and one output and consists of one input layer (Layer 0) and one output layer (Layer 2) each with identity activation function $\Phi_0(y) = \Phi_2(y) = \Phi_{\mathrm{id}}(y) = y$. The one hidden layer (Layer 1) comes with two (for RSMs) or three (for IPMSMs) neurons and utilizes special activation functions $\Phi_{1,1}(y_1, y_2) = \Phi_{1,2}(y_1, y_2) = \Phi_{1,3}(y_1, y_2) = \Phi'_{\mathrm{m}}(y_1)\Phi_{\mathrm{m}}(y_2)$ for the d-axis and $\Phi_{\mathrm{m}}(y_1)\Phi'_{\mathrm{m}}(y_2)$ for the q-axis of machine $\mathrm{m} \in \{\mathrm{ipmsm}, \mathrm{rsm}\}$, respectively. Hence, one obtains

$$\widehat{\psi}^d_{\mathrm{s,cross}}(i^d_{\mathrm{s}}, i^q_{\mathrm{s}}) = \sum_{i=1}^{n} w^{\mathrm{cross}}_{2,i} \Phi'_{\mathrm{m}}\big(i^d_{\mathrm{s}}\big)\Phi_{\mathrm{m}}\big(i^q_{\mathrm{s}}\big) \tag{21}$$

$$\widehat{\psi}^q_{\mathrm{s,cross}}(i^d_{\mathrm{s}}, i^q_{\mathrm{s}}) = \sum_{i=1}^{n} w^{\mathrm{cross}}_{2,i} \Phi_{\mathrm{m}}\big(i^d_{\mathrm{s}}\big)\Phi'_{\mathrm{m}}\big(i^q_{\mathrm{s}}\big) \tag{22}$$

such that $L^{dq}_{\mathrm{s}} = \frac{\partial \psi^d_{\mathrm{s,cross}}(i^d_{\mathrm{s}}, i^q_{\mathrm{s}})}{\partial i^q_{\mathrm{s}}} = \frac{\partial \psi^q_{\mathrm{s,cross}}(i^d_{\mathrm{s}}, i^q_{\mathrm{s}})}{\partial i^d_{\mathrm{s}}} = L^{qd}_{\mathrm{s}}$ and conservation of energy [34] is also assured by the approximation of the cross-axis flux linkages, i.e.

$$\frac{\partial \widehat{\psi}^d_{\mathrm{s,cross}}(i^d_{\mathrm{s}}, i^q_{\mathrm{s}})}{\partial i^q_{\mathrm{s}}} = \frac{\partial \widehat{\psi}^q_{\mathrm{s,cross}}(i^d_{\mathrm{s}}, i^q_{\mathrm{s}})}{\partial i^d_{\mathrm{s}}} = \sum_{i=1}^{n} w^{\mathrm{cross}}_{2,i} \Phi'_{\mathrm{m}}\big(i^d_{\mathrm{s}}\big)\Phi'_{\mathrm{m}}\big(i^q_{\mathrm{s}}\big).$$

For IPMSMs (i.e., $\mathrm{m} = \mathrm{ipmsm}$), in (21) and (22), we set $n = 3$ and choose $\Phi_{\mathrm{m}}(y) = \Phi_{\mathrm{ipmsm}}(y) := y + y^2 + \ln\big(1 + \exp(y)\big)$ with $\Phi'_{\mathrm{m}}(y) = \Phi'_{\mathrm{ipmsm}}(y) = 1 + 2y + \frac{1}{1+\exp(-y)}$ (weights and biases omitted) which leads to (23).

For RSMs (i.e., $\mathrm{m} = \mathrm{rsm}$), in (21) and (22), we set $n = 2$ and choose $\Phi_{\mathrm{m}}(y) = \Phi_{\mathrm{rsm}}(y) := 1 - \exp(-y^2)$ with $\Phi'_{\mathrm{m}}(y) = \Phi'_{\mathrm{rsm}}(y) = 2y\exp(-y^2)$ (motivated by [34]; again weights and biases omitted) which yields (24).

D. Approximation of differential inductances

According to (10), the differential inductances are the partial derivatives of the flux linkages with respect to the currents. In view of (16), those can be directly approximated by

$$\begin{pmatrix} \widehat{L}^{dd}_{\mathrm{s}}(i^d_{\mathrm{s}}, i^q_{\mathrm{s}}) \\ \widehat{L}^{qq}_{\mathrm{s}}(i^d_{\mathrm{s}}, i^q_{\mathrm{s}}) \end{pmatrix} = \begin{pmatrix} \frac{\partial \widehat{\psi}^d_{\mathrm{s,self}}(i^d_{\mathrm{s}})}{\partial i^d_{\mathrm{s}}} \\ \frac{\partial \widehat{\psi}^q_{\mathrm{s,self}}(i^q_{\mathrm{s}})}{\partial i^q_{\mathrm{s}}} \end{pmatrix} + \begin{pmatrix} \frac{\partial \widehat{\psi}^d_{\mathrm{s,cross}}(i^d_{\mathrm{s}}, i^q_{\mathrm{s}})}{\partial i^d_{\mathrm{s}}} \\ \frac{\partial \widehat{\psi}^q_{\mathrm{s,cross}}(i^d_{\mathrm{s}}, i^q_{\mathrm{s}})}{\partial i^q_{\mathrm{s}}} \end{pmatrix} \tag{25}$$

and

$$\widehat{L}^{dq}_{\mathrm{s}}(i^d_{\mathrm{s}}, i^q_{\mathrm{s}}) = \frac{\partial \widehat{\psi}^d_{\mathrm{s,cross}}(i^d_{\mathrm{s}}, i^q_{\mathrm{s}})}{\partial i^q_{\mathrm{s}}} = \frac{\partial \widehat{\psi}^q_{\mathrm{s,cross}}(i^d_{\mathrm{s}}, i^q_{\mathrm{s}})}{\partial i^d_{\mathrm{s}}} = \widehat{L}^{qd}_{\mathrm{s}}(i^d_{\mathrm{s}}, i^q_{\mathrm{s}}) \tag{26}$$

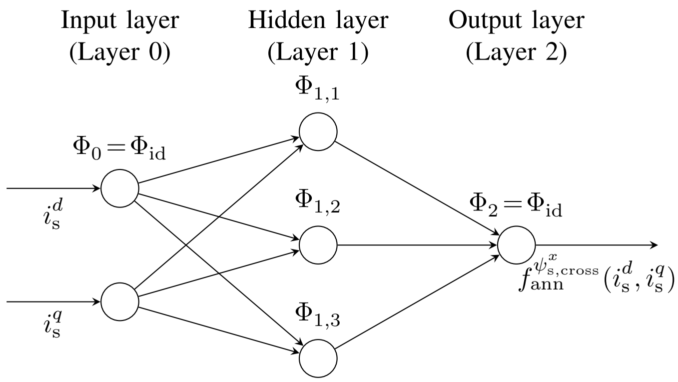

Figure 4: ANN for approximation of cross-axis flux linkage $\psi^x_{\mathrm{s,cross}}(i_{\mathrm{s}}^d, i_{\mathrm{s}}^q)$ of axis $x \in \{d, q\}$ by $\widehat{\psi}^x_{\mathrm{s,cross}}(i_{\mathrm{s}}^d, i_{\mathrm{s}}^q) := f_{\mathrm{ann}}^{\psi^x_{\mathrm{s,cross}}}(i_{\mathrm{s}}^d, i_{\mathrm{s}}^q)$.

with the help of the ANN-based flux linkage estimates in (17) and (20). As the computation of the partial derivatives of (18), (19), (23) and (24) is lengthy but straightforward, the explicit expressions of the differential inductance approximations are omitted due to space limitations.

IV. Overall Identification Algorithm

The proposed identification consists of three parts: (P1) a rotor alignment and locking procedure (at least for a q-axis characterisation); (P2) a special open-loop voltage excitation of the machine under test (MUT) at standstill for a fraction of a second or a few seconds; and (P3) a post-processing identification method which solves a recursive least squares optimization problem offline (for details see [37, Section 4.2 & 10.4.5] or [31]). The three parts will be discussed in more detail in the following.

A. Rotor alignment and standstill operation (P1)

At the beginning of the identification process, the machine is excited in α-axis direction with a constant reference voltage magnitude to align the machine rotor with the d-axis in order to achieve $\phi_{\mathrm{p}} \approx 0^\circ$. Next, the reference voltage is slowly increased until a pre-defined maximum (e.g., rated) current is obtained in order to guarantee correct alignment (i.e. $\phi_{\mathrm{p}} = 0^\circ$). Then, the rotor is mechanically locked. Alternatively, one can directly lock the rotor and apply a high-frequency position estimation technique [38]. Afterwards, the self-axis and cross-axis identification is conducted with the following two steps:

(S1) Open-loop excitation (for self-axis identification, d and q-axis are excited separately; whereas for cross-coupling identification, both axes are excited simultaneously).

(S2) Post-processing identification (the obtained weights during self-axis identification serve as initial weights for cross-axis identification).

Both steps are explained in more detail in the following.

B. Open-loop excitation (P2)

For a simultaneous estimation of all ANN parameters of the VSI and machine model, a "sufficiently rich" excitation signal must be applied to produce current responses within the high- and low-current region (see Fig. 1). From a system theoretical point of view, one must assure "persistency of excitation" [39], which, according to the applied voltage steps due to the switching nature of the inverter, is guaranteed as steps contain (theoretically) infinitely many frequencies. Moreover, properly chosen and varying excitation (reference) voltages (see (27)) in combination with the nonlinear phase voltage deviations Δu_{s}^p as in (4) excite the current dynamics additionally. To improve the richness of the excitation signal further and to distinguish during steady-state operation of the current response between a voltage drop caused by Δu_{s}^p and a voltage drop over the stator resistance R_{s}, the excitation magnitude should vary e.g. after a full excitation period $\frac{1}{f_{\mathrm{ext}}}$ (see Sec. V-B), such that a steady-state current response is guaranteed within the high-current *and* the low-current region. In conclusion, a proper excitation signal in the (d, q)-reference frame must be chosen

$$u_{\mathrm{s,ref}}^{d/q}(t) = \begin{cases} \overline{u}_{\mathrm{sat}}(t), & \text{if } u_{\mathrm{ext}}(t) \geq \overline{u}_{\mathrm{sat}}(t) \\ \underline{u}_{\mathrm{sat}}(t), & \text{if } u_{\mathrm{ext}}(t) \leq \underline{u}_{\mathrm{sat}}(t) \\ \underbrace{a_{\mathrm{ext}}(t)\sin\left(2\pi f_{\mathrm{ext}} t\right)}_{=:u_{\mathrm{ext}}(t)}, & \text{else,} \end{cases} \tag{27}$$

where $a_{\mathrm{ext}}(t)$, $\underline{u}_{\mathrm{sat}}(t)$ and $\overline{u}_{\mathrm{sat}}(t)$ may change after each excitation period to allow for different amplitudes and lower and upper saturation levels of the test signal to avoid over-currents and to force different steady-state responses.

As a rule of thumb, (at least) two cycles of (27) should be applied: One cycle for the high-current region and one cycle for the low-current region. Each cycle should contain at least 100 samples where at least $N_{\min} = 50$ samples for steady state and transient response should be recorded, respectively. The following steps to obtain a proper parametrisation of (27) are recommended: (i) The α/d-axis phase voltage is ramped up, e.g. by $+1\,\frac{\mathrm{V}}{\mathrm{s}}$, until a predefined maximum current is reached, e.g., $I_{\max} = I_{\mathrm{R}}$ (rated current). The corresponding maximum voltage for $I_{\max}$ is stored as $\overline{u}_{\mathrm{sat}}$ and prevents further over-currents. The same procedure can be repeated for the low-current region with e.g. $I_{\max} = 2.5\,\mathrm{A}$ (see Fig. 1); (ii) the excitation signal in (27) now can be pre-parametrised for the high-current and the low-current region with $\overline{u}_{\mathrm{sat}}$, $a_{\mathrm{ext}} = \overline{u}_{\mathrm{sat}}$ and $f_{\mathrm{ext}} = f_{\mathrm{R}}$ (rated machine frequency), respectively; (iii) afterwards f_{ext} is reduced, e.g. by $-1\,\frac{\mathrm{Hz}}{\mathrm{s}}$, until the measured currents reach their respective limit $I_{\max}$ in both current regions; and (iv) a_{ext} is increased again until at least $N_{\min}$ samples are obtained for steady state and transient current response, respectively. Finally, all parameters for high-current and low-current region are stored and two cycles of the excitation signal (27) are applied.

C. Post-processing identification (P3)

Goal is to find an expression which allows to identify all parameters of the ANNs simultaneously only based on the current measurements $\boldsymbol{i}_{\mathrm{s}}^{dq}[n]$ and the applied (reference) voltages $\boldsymbol{u}_{\mathrm{s,ref}}^{dq}[n]$ for a set of samples $n \in \{0, 1, \ldots, N\}$ (where 0 represents the initial time step and $N \gg 1$ is large). To do so, the current dynamics in (13) in combination with

$$\text{IPMSMs:}\left\{\begin{array}{rcl} \widehat{\psi}^d_{\mathrm{s,cross}}(i^d_{\mathrm{s}}, i^q_{\mathrm{s}}) & = & w^{\mathrm{cross}}_{2,1}\Big(w^{d,\mathrm{cross}}_{1,1,1} + 2w^{d,\mathrm{cross}}_{1,1,2}\, i^d_{\mathrm{s}} + \frac{w^{d,\mathrm{cross}}_{1,1,3}}{1+\exp(-(i^d_{\mathrm{s}}+b^{d,\mathrm{cross}}_{1,1}))}\Big)\cdot \\ & & \quad \Big(w^{q,\mathrm{cross}}_{1,1,1}\, i^q_{\mathrm{s}} + w^{q,\mathrm{cross}}_{1,1,2}(i^q_{\mathrm{s}})^2 + w^{q,\mathrm{cross}}_{1,1,3}\ln\big(\exp(i^q_{\mathrm{s}} + b^{q,\mathrm{cross}}_{1,1}) + 1\big)\Big) \\ & & +w^{\mathrm{cross}}_{2,2}\Big(w^{d,\mathrm{cross}}_{1,2,1} + 2w^{d,\mathrm{cross}}_{1,2,2}\, i^d_{\mathrm{s}} + \frac{w^{d,\mathrm{cross}}_{1,2,3}}{1+\exp(-(i^d_{\mathrm{s}}+b^{d,\mathrm{cross}}_{1,2}))}\Big)\cdot \\ & & \quad \Big(w^{q,\mathrm{cross}}_{1,2,1}\, i^q_{\mathrm{s}} + w^{q,\mathrm{cross}}_{1,2,2}(i^q_{\mathrm{s}})^2 + w^{q,\mathrm{cross}}_{1,2,3}\ln\big(\exp(i^q_{\mathrm{s}} + b^{q,\mathrm{cross}}_{1,2}) + 1\big)\Big) \\ & & +w^{\mathrm{cross}}_{2,3}\Big(w^{d,\mathrm{cross}}_{1,3,1} + 2w^{d,\mathrm{cross}}_{1,3,2}\, i^d_{\mathrm{s}} + \frac{w^{d,\mathrm{cross}}_{1,3,3}}{1+\exp(-(i^d_{\mathrm{s}}+b^{d,\mathrm{cross}}_{1,3}))}\Big)\cdot \\ & & \quad \Big(w^{q,\mathrm{cross}}_{1,3,1}\, i^q_{\mathrm{s}} + w^{q,\mathrm{cross}}_{1,3,2}(i^q_{\mathrm{s}})^2 + w^{q,\mathrm{cross}}_{1,3,3}\ln\big(\exp(i^q_{\mathrm{s}} + b^{q,\mathrm{cross}}_{1,3}) + 1\big)\Big) \\ \widehat{\psi}^q_{\mathrm{s,cross}}(i^d_{\mathrm{s}}, i^q_{\mathrm{s}}) & = & w^{\mathrm{cross}}_{2,1}\Big(w^{q,\mathrm{cross}}_{1,1,1} + 2w^{q,\mathrm{cross}}_{1,1,2}\, i^q_{\mathrm{s}} + \frac{w^{q,\mathrm{cross}}_{1,1,3}}{1+\exp(-(i^q_{\mathrm{s}}+b^{q,\mathrm{cross}}_{1,1}))}\Big)\cdot \\ & & \quad \Big(w^{d,\mathrm{cross}}_{1,1,1}\, i^d_{\mathrm{s}} + w^{d,\mathrm{cross}}_{1,1,2}(i^d_{\mathrm{s}})^2 + w^{d,\mathrm{cross}}_{1,1,3}\ln\big(\exp(i^d_{\mathrm{s}} + b^{d,\mathrm{cross}}_{1,1}) + 1\big)\Big) \\ & & +w^{\mathrm{cross}}_{2,2}\Big(w^{q,\mathrm{cross}}_{1,2,1} + 2w^{q,\mathrm{cross}}_{1,2,2}\, i^q_{\mathrm{s}} + \frac{w^{q,\mathrm{cross}}_{1,2,3}}{1+\exp(-(i^q_{\mathrm{s}}+b^{q,\mathrm{cross}}_{1,2}))}\Big)\cdot \\ & & \quad \Big(w^{d,\mathrm{cross}}_{1,2,1}\, i^d_{\mathrm{s}} + w^{d,\mathrm{cross}}_{1,2,2}(i^d_{\mathrm{s}})^2 + w^{d,\mathrm{cross}}_{1,2,3}\ln\big(\exp(i^d_{\mathrm{s}} + b^{d,\mathrm{cross}}_{1,2}) + 1\big)\Big) \\ & & +w^{\mathrm{cross}}_{2,3}\Big(w^{q,\mathrm{cross}}_{1,3,1} + 2w^{q,\mathrm{cross}}_{1,3,2}\, i^q_{\mathrm{s}} + \frac{w^{q,\mathrm{cross}}_{1,3,3}}{1+\exp(-(i^q_{\mathrm{s}}+b^{d,\mathrm{cross}}_{1,3}))}\Big)\cdot \\ & & \quad \Big(w^{d,\mathrm{cross}}_{1,3,1}\, i^d_{\mathrm{s}} + w^{d,\mathrm{cross}}_{1,3,2}(i^d_{\mathrm{s}})^2 + w^{d,\mathrm{cross}}_{1,3,3}\ln\big(\exp(i^d_{\mathrm{s}} + b^{d,\mathrm{cross}}_{1,3}) + 1\big)\Big). \end{array}\right\} \tag{23}$$

$$\text{RSMs:}\left\{\begin{array}{rcl} \widehat{\psi}^d_{\mathrm{s,cross}}(i^d_{\mathrm{s}}, i^q_{\mathrm{s}}) & = & 2w^{\mathrm{cross}}_{2,1}(w^{d,\mathrm{cross}}_{1,1})^2 i^d_{\mathrm{s}} \exp\Big(-(w^{d,\mathrm{cross}}_{1,1} i^d_{\mathrm{s}})^2\Big)\Big(1-\exp\Big(-(w^{q,\mathrm{cross}}_{1,1} i^q_{\mathrm{s}})^2\Big)\Big) \\ & & +2w^{\mathrm{cross}}_{2,2}(w^{d,\mathrm{cross}}_{1,2})^2 i^d_{\mathrm{s}} \exp\Big(-(w^{d,\mathrm{cross}}_{1,2} i^d_{\mathrm{s}})^2\Big)\Big(1-\exp\Big(-(w^{q,\mathrm{cross}}_{1,2} i^q_{\mathrm{s}})^2\Big)\Big) \\ \widehat{\psi}^q_{\mathrm{s,cross}}(i^d_{\mathrm{s}}, i^q_{\mathrm{s}}) & = & 2w^{\mathrm{cross}}_{2,1}(w^{q,\mathrm{cross}}_{1,1})^2 i^q_{\mathrm{s}} \exp\Big(-(w^{q,\mathrm{cross}}_{1,1} i^q_{\mathrm{s}})^2\Big)\Big(1-\exp\Big(-(w^{d,\mathrm{cross}}_{1,1} i^d_{\mathrm{s}})^2\Big)\Big) \\ & & +2w^{\mathrm{cross}}_{2,2}(w^{q,\mathrm{cross}}_{1,2})^2 i^q_{\mathrm{s}} \exp\Big(-(w^{q,\mathrm{cross}}_{1,2} i^q_{\mathrm{s}})^2\Big)\Big(1-\exp\Big(-(w^{d,\mathrm{cross}}_{1,2} i^d_{\mathrm{s}})^2\Big)\Big). \end{array}\right\} \tag{24}$$

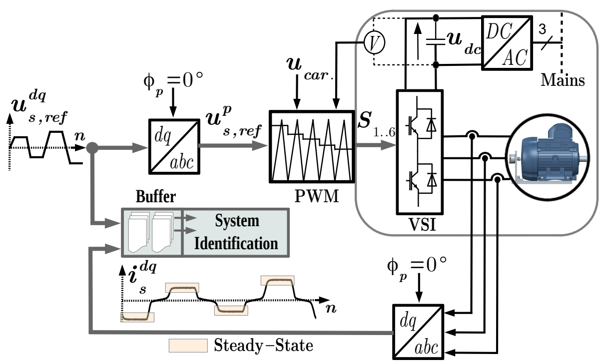

Figure 5: Simplified block diagram of the excitation and identification process.

the proposed ANNs can be used to compute the estimated currents $\widehat{\boldsymbol{i}}^{dq}_{\mathrm{s}}[n]$ for each sampled time instant of the recorded measurements. As only currents and voltage references are available for identification, the actual voltages $\boldsymbol{u}^{dq}_{\mathrm{s}}[n]$ in (13) must be replaced by $\boldsymbol{u}^{dq}_{\mathrm{s,ref}}[n] - \Delta\boldsymbol{u}^{dq}_{\mathrm{s}}[n]$ as in (4), which yields

$$\boldsymbol{i}^{dq}_{\mathrm{s}}[n+1] \approx \boldsymbol{A}^{dq}_{\mathrm{s}}[n]\boldsymbol{i}^{dq}_{\mathrm{s}}[n] + \boldsymbol{B}^{dq}_{\mathrm{s}}[n]\Big(\boldsymbol{u}^{dq}_{\mathrm{s,ref}}[n] - \Delta\boldsymbol{u}^{dq}_{\mathrm{s}}[n]\Big).$$

Moreover, the entries of the matrices $\boldsymbol{A}^{dq}_{\mathrm{s}}[n]$ and $\boldsymbol{B}^{dq}_{\mathrm{s}}[n]$ are not a priori known and, actually, depend on T_{s}, $L^{dd}_{\mathrm{s}}(\boldsymbol{i}^{dq}_{\mathrm{s}}[n])$, $L^{qq}_{\mathrm{s}}(\boldsymbol{i}^{dq}_{\mathrm{s}}[n])$, $L^{dq}_{\mathrm{s}}(\boldsymbol{i}^{dq}_{\mathrm{s}}[n])$ and R_{s}. Hence, those and also the unknown inverter nonlinearities $\Delta\boldsymbol{u}^{dq}_{\mathrm{s}}$ need to be replaced by their estimates $\widehat{\boldsymbol{A}}^{dq}_{\mathrm{s}}[n] := \boldsymbol{I}_2 - \widehat{R}_{\mathrm{s}} T_{\mathrm{s}} \widehat{\boldsymbol{L}}^{dq}_{\mathrm{s}}(\boldsymbol{i}^{dq}_{\mathrm{s}}[n])^{-1}$, $\widehat{\boldsymbol{B}}^{dq}_{\mathrm{s}}[n] := T_{\mathrm{s}}\widehat{\boldsymbol{L}}^{dq}_{\mathrm{s}}(\boldsymbol{i}^{dq}_{\mathrm{s}}[n])^{-1}$ and $\Delta\widehat{\boldsymbol{u}}^{dq}_{\mathrm{s}}$, respectively, to predict

$$\widehat{\boldsymbol{i}}^{dq}_{\mathrm{s}}[n+1] \approx \widehat{\boldsymbol{A}}^{dq}_{\mathrm{s}}[n]\boldsymbol{i}^{dq}_{\mathrm{s}}[n] + \widehat{\boldsymbol{B}}^{dq}_{\mathrm{s}}[n]\Big(\boldsymbol{u}^{dq}_{\mathrm{s,ref}}[n] - \Delta\widehat{\boldsymbol{u}}^{dq}_{\mathrm{s}}[n]\Big) \tag{28}$$

at the next sampling instant where the estimated VSI nonlinearities as in (8) and estimated differential inductance matrix

$$\widehat{\boldsymbol{L}}^{dq}_{\mathrm{s}}(\boldsymbol{i}^{dq}_{\mathrm{s}}[n]) \overset{(18)}{=} \begin{bmatrix} \overbrace{\frac{\partial f^{\psi,d}_{\mathrm{ann}}(\boldsymbol{i}^{dq}_{\mathrm{s}}[n])}{\partial i^d_{\mathrm{s}}}}^{=:\widehat{L}^{dd}_{\mathrm{s}}(\boldsymbol{i}^{dq}_{\mathrm{s}}[n])} & \overbrace{\frac{\partial f^{\psi,d}_{\mathrm{ann}}(\boldsymbol{i}^{dq}_{\mathrm{s}}[n])}{\partial i^q_{\mathrm{s}}}}^{=:\widehat{L}^{dq}_{\mathrm{s}}(\boldsymbol{i}^{dq}_{\mathrm{s}}[n])} \\ \underbrace{\frac{\partial f^{\psi,q}_{\mathrm{ann}}(\boldsymbol{i}^{dq}_{\mathrm{s}}[n])}{\partial i^d_{\mathrm{s}}}}_{=:\widehat{L}^{qd}_{\mathrm{s}}(\boldsymbol{i}^{dq}_{\mathrm{s}}[n])} & \underbrace{\frac{\partial f^{\psi,q}_{\mathrm{ann}}(\boldsymbol{i}^{dq}_{\mathrm{s}}[n])}{\partial i^q_{\mathrm{s}}}}_{:=\widehat{L}^{qq}_{\mathrm{s}}(\boldsymbol{i}^{dq}_{\mathrm{s}}[n])} \end{bmatrix}$$

(and, hence, also its inverse $\widehat{\boldsymbol{L}}^{dq}_{\mathrm{s}}(\boldsymbol{i}^{dq}_{\mathrm{s}}[n])^{-1}$) can be expressed with the help of the proposed ANNs as in (6), (18), (19), (23), (24), respectively. Finally, collecting (i) the identification parameters of the (to be estimated) stator resistance $\widehat{R}^x_{\mathrm{s}}$ and the weights and biases of the ANNs in one parameter vector

$$\boldsymbol{\theta}_{\mathrm{s}} := \big(\widehat{R}^x_{\mathrm{s}}, w^{\mathrm{vsi}}_{1,1}, \ldots, b^{\mathrm{vsi}}_{1,2}, \ldots, w^{d/q,\mathrm{self}}_{1,1}, \ldots, w^{d/q,\mathrm{cross}}_{1,1,1/1,1}, \ldots,\big)^\top$$

and (ii) the $N{+}1$ samples of the currents $\boldsymbol{i}^{dq}_{\mathrm{s}}[0], \ldots, \boldsymbol{i}^{dq}_{\mathrm{s}}[N]$ and voltage references $\boldsymbol{u}^{dq}_{\mathrm{s,ref}}[0], \ldots, \boldsymbol{u}^{dq}_{\mathrm{s,ref}}[N]$ during the open-loop excitation allows to rewrite, for all $n \in \{0, \ldots, N-1\}$, the estimated current dynamics as

$$\widehat{\boldsymbol{i}}^{dq}_{\mathrm{s}}[n+1] = \boldsymbol{f}(\boldsymbol{i}^{dq}_{\mathrm{s}}[n], \boldsymbol{u}^{dq}_{\mathrm{s,ref}}[n], \boldsymbol{\theta}_{\mathrm{s}}),$$

which only depends on $\boldsymbol{i}_{\rm s}^{dq}[n]$, $\boldsymbol{u}_{\rm s,ref}^{dq}[n]$ and $\boldsymbol{\theta}_{\rm s}$ and can directly be computed with (28). Hence, an optimization problem

$$\boldsymbol{\theta}_{\rm s}^{\star} := \arg\min_{\boldsymbol{\theta}_{\rm s}} \left\| \begin{pmatrix} \boldsymbol{i}_{\rm s}^{dq}[1] - \widehat{\boldsymbol{i}}_{\rm s}^{dq}[1] \\ \vdots \\ \boldsymbol{i}_{\rm s}^{dq}[N] - \widehat{\boldsymbol{i}}_{\rm s}^{dq}[N] \end{pmatrix} \right\|^2 \tag{29}$$

can be formulated and solved by the Levenberg-Marquardt algorithm or any Particle Swarm Optimization (PSO) algorithm which yields the optimal parameter vector $\boldsymbol{\theta}_{\rm s}^{\star}$ including the estimated stator resistance and the weights and biases of both ANNs for d and q axes. Evaluating the trained ANNs for different currents allows to approximate (i) the VSI voltage deviations $\widehat{u}_{\rm s}^{p}(i_{\rm s}^{p}) = f_{\rm ann}^{\rm vsi}(i_{\rm s}^{p})$ as in (6) with $p \in \{a, b, c\}$, (ii) the self-axis flux linkages $\widehat{\psi}_{\rm s,self}^{x}(i_{\rm s}^{x}) = f_{\rm ann}^{\psi_{\rm s,self}^{x}}(i_{\rm s}^{x})$ as in (18) or (19), (iii) the cross-axis flux linkages $\widehat{\psi}_{\rm s,cross}^{x}(i_{\rm s}^{d}, i_{\rm s}^{q}) = f_{\rm ann}^{\psi_{\rm s,cross}^{x}}(i_{\rm s}^{d}, i_{\rm s}^{q})$ as in (23) for IPMSMs and (24) for RSMs, and (iv) the differential inductances $\widehat{L}_{\rm s}^{dd}(i_{\rm s}^{d}, i_{\rm s}^{q})$, $\widehat{L}_{\rm s}^{qq}(i_{\rm s}^{d}, i_{\rm s}^{q})$ and $\widehat{L}_{\rm s}^{dq}(i_{\rm s}^{d}, i_{\rm s}^{q}) = \widehat{L}_{\rm s}^{qd}(i_{\rm s}^{d}, i_{\rm s}^{q})$ as in (25) and (26).

Remark 6. *Usually the electrical drive system exhibits a time delay T_Σ comprising delays due to sample and hold circuits of the digital control environment, pulse width modulation (PWM), inverter and analogue-to-digital conversion [2]. For $\frac{1}{f_{ext}} \gg T_\Sigma$ (see Table II), the system delay is negligible. If this is not the case, one needs to estimate T_Σ during the identification as additional parameter or, if T_Σ is known, $u_{\rm s,ref}^{d/q}[n]$ must be shifted accordingly during post-processing [2].*

V. Experimental validation

A. Description of experimental setup

The proposed identification method, as illustrated in Fig. 5, was implemented on a Cyclone IV (EP4CE22F17C6N) field programmable gate array (FPGA) with the help of a rapid prototyping system for model-based controller design. The test bench consists of a three-phase two-level inverter with Semikron SKM50GB12T4 insulated-gate bipolar transistors (IGBTs) rated for 50 A and 1200 V operating at a switching frequency of $f_{\rm sw} = 10\,\rm kHz$ with a dead time of $3\mu s$. The phase currents were measured by a 12-bit 60 kHz analogue to digital converter using LEM HXS 20-NP Hall sensors.

Table I: Considered machines and key data.

Machine Type	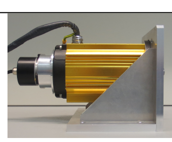 **M1: IPMSM**	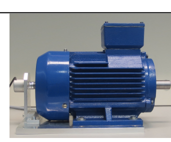 **M2: RSM**
Manufacturer	EMP	Stellenbosch [40]
Designation	Prototype	Prototype
Rated Phase Current $I_{\rm R}$	$4.07\,\rm A_{rms}$	$3.54\,\rm A_{rms}$
Rated Torque $m_{\rm m,R}$	2.06 N m	9.60 N m
Poles	8 ($n_{\rm p} = 4$)	4 ($n_{\rm p} = 2$)
Rated Speed $n_{\rm m,R}$	6000 rpm	1500 rpm

The proposed identification is demonstrated for an IPMSM and an RSM with nominal ratings as shown in Table I. The DC-link voltage was permanently set to $u_{\rm dc} = 300\,\rm V$. Due to that, the VSI voltage deviations $\Delta u_{\rm s}^{p}(i_{\rm s}^{p})$ and, therefore, also their approximations $\Delta\widehat{u}_{\rm s}^{p}(i_{\rm s}^{p})$ in (6) are expected to be very similar for IPMSM and RSM identification. Small deviation in the low current region are possible due to the dependence on the output capacitance of the VSI legs resulting in a varying off time as in (3) [9], [12].

The experimental settings, such as parameters of the excitation signal (27) composed of $\underline{u}_{\rm sat}(t)$, $\overline{u}_{\rm sat}(t)$, $a_{\rm ext}(t)$ and $f_{\rm ext}$ and other implementation data, are collected in Table II. The excitation voltage can be obtained by gradually increasing $a_{\rm ext}(t)$, $-\underline{u}_{\rm sat}(t)$ and $\overline{u}_{\rm sat}(t)$ until a desired current (e.g., three times the rated current) is reached in steady state. Solely, the rated current, voltage and frequency must be known for the identification but can usually be extracted from the nameplate. For the following experiments, the parameters of the excitation signal were obtained by trial and error but could also be obtained by an automated process within a high-level logic in the operating system of the electrical drive. The automated choice of proper excitation signals is still an open research question (e.g., also for other stand-still methods, see [24]) and is not considered in this paper (future research).

Table II: Experimental settings for identification.

	IPMSM		RSM	
Self-axis identification	**d-axis**	**q-axis**	**d-axis**	**q-axis**
Excitation amplitude $a_{\rm ext}$	25 V	25 V	90 V	90 V
Saturation $\overline{u}_{\rm sat} = -\underline{u}_{\rm sat}$	[17, 12]V	[17, 12]V	[54, 27]V	[54, 27]V
Excitation frequency $f_{\rm ext}$	5 Hz	5 Hz	1 Hz	5 Hz
Sampling frequency $f_{\rm s}$	10 kHz	10 kHz	1 kHz	5 kHz
Switching frequency $f_{\rm sw}$	10 kHz	10 kHz	10 kHz	10 kHz
Samples N per signal (29)	4096	4096	4096	4096
Cross-axis identification	**d-axis**	**q-axis**	**d-axis**	**q-axis**
Excitation amplitude $a_{\rm ext}$	25 V	25 V	90 V	90 V
Saturation $\overline{u}_{\rm sat} = -\underline{u}_{\rm sat}$	[17, 12]V	[17, 11]V	[54, 27]V	[54, 27]V
Excitation frequency $f_{\rm ext}$	5 Hz	20 Hz	1 Hz	10 Hz
Sampling frequency $f_{\rm s}$	5 kHz	5 kHz	1 kHz	1 kHz
Switching frequency $f_{\rm sw}$	10 kHz	10 kHz	10 kHz	10 kHz
Samples N per signal (29)	2048	2048	2048	2048

B. Discussion of experimental results

The identification results are shown in Fig. 6 and 7 for the IPMSM, in Fig. 8 and 9 for the RSM and in Fig. 10 for the VSI. The identified model parameters and phase resistance estimation results and references are listed in Tab. III.

In Fig. 6, the self-axis identification results and, in Fig. 7, the cross-axis (full) identification results for the IPMSM are presented. The first subplot (a) of Fig. 6 and Fig. 7 show the time series of excitation signal $u_{\rm s,ref}^{d/q}$ with respective actual $i_{\rm s}^{d/q}$ and predicted current $\widehat{i}_{\rm s}^{d/q}$ responses according to (28). Subplots (b) & (c) of Fig. 6 and of Fig. 7 show actual and identified self-axis flux linkage curves and flux linkage maps, respectively. Subplots (d) & (e) of Fig. 6 show actual $L_{\rm s}^{dd/qq}$ and identified $\widehat{L}_{\rm s}^{dd/qq}$ (self-axis) differential inductances of the IPMSM, whereas subplots (d) & (e) of Fig. 7 show the relative flux linkage map errors of the cross-axis (full) identification.

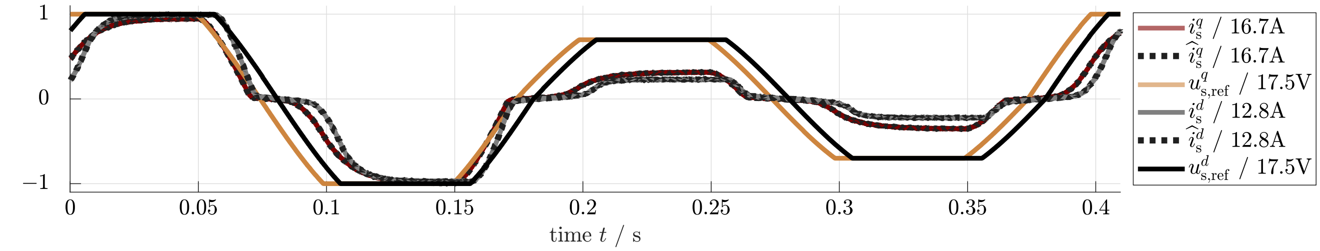

(a) Time series of the normalized stator d- and q-axis current and its estimate and stator voltage references.

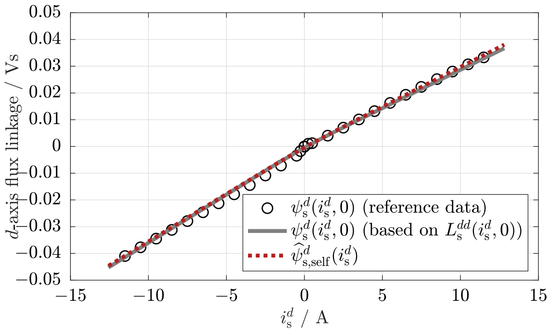

(b) Comparison of d-axis flux linkage $\psi_s^d(i_s^d, 0)$ and its self-axis estimate $\widehat{\psi}_{s,self}^d(i_s^d) = f_{ann}^{\psi,d}(i_s^d)$.

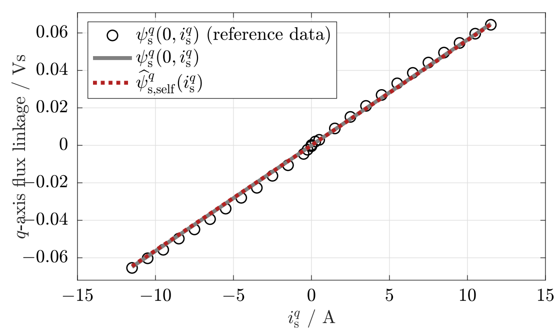

(c) Comparison of q-axis flux linkage $\psi_s^q(0, i_s^q)$ and its self-axis estimate $\widehat{\psi}_{s,self}^q(i_s^q) = f_{ann}^{\psi,q}(i_s^q)$.

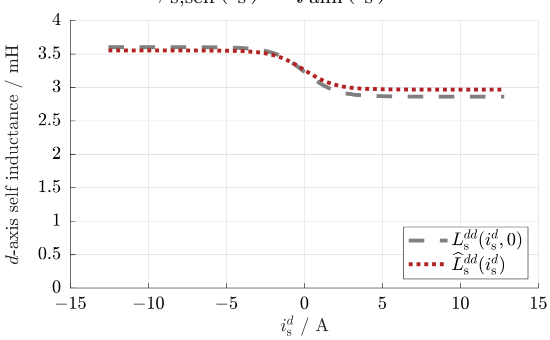

(d) Comparison of d-axis self inductance $L_s^{dd}(i_s^d, 0)$ and its estimate $\widehat{L}_s^{dd}(i_s^d) = \frac{\partial \widehat{\psi}_{s,self}^d(i_s^d)}{\partial i_s^d}$.

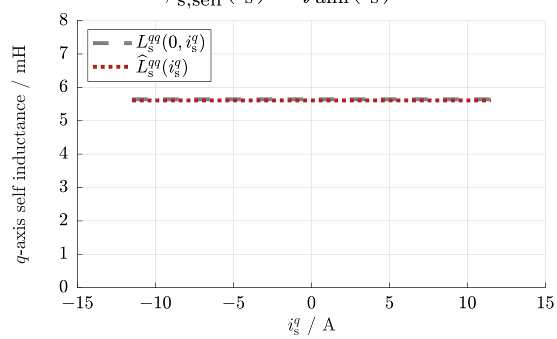

(e) Comparison of q-axis self inductance $L_s^{qq}(0, i_s^q)$ and its estimate $\widehat{L}_s^{qq}(i_s^q) = \frac{\partial \widehat{\psi}_{s,self}^q(i_s^q)}{\partial i_s^q}$.

Figure 6: **IPMSM identification results:** (a) Time series; (b) & (c) self-axis flux linkages; (d) & (e) differential inductances.

The actual (reference) measurements were obtained from the CSM [6]. It can be seen, that the self-axis flux linkages and inductances and the flux linkage maps were identified with good accuracy and small relative errors of -8% to 2% for $\widehat{\psi}_s^d(i_s^d, i_s^q)$ and -6% to 5% for $\widehat{\psi}_s^q(i_s^d, i_s^q)$. A small deviation can also be seen in the d-axis differential inductance which is due to the asymmetry of the d-axis flux linkage which is particularly dominant within the zero current region of an IPMSM as a result of the permanent magnet [34]. A more accurate representation within this region requires usually a significantly increased model complexity as for which it is often omitted (such as in [16]). The bias $b_2^{q,\text{self}}$ as shown in Tab. III is zero due to the absence of a q-axis permanent magnet flux linkage. Fig. 8 and Fig. 9 illustrate the self-axis and cross-axis (full) identification results for the RSM, respectively. Again, time series, self-axis flux linkage curves or flux linkage maps and self-axis differential inductances or relative flux linkage errors for the d- and q-axis are shown in subplots (a), (b) & (c) and (d) & (e), respectively. The actual (reference) data of flux linkages and differential inductances was taken from [6]. It can be seen, that the self-axis flux linkage curves and self-axis differential inductance curves were identified with high accuracy. Also, the identified flux linkage maps exhibit (very) small relative errors of -4% to 3% for $\widehat{\psi}_s^d(i_s^d, i_s^q)$ and -4% to 6% for $\widehat{\psi}_s^q(i_s^d, i_s^q)$. Fig. 10 shows the identification results of the VSI voltage deviations for the IPMSM and RSM. It can be seen that reference and estimation do match very accurately, i.e., $\Delta u_s^{d/q}(i_s^{d/q}) \approx \Delta \widehat{u}_s^{d/q}(i_s^{d/q})$ with errors less than $0.179\,\text{V}$ (2.2%) to $0.320\,\text{V}$ (4.0%) with respect to the high current region voltage error. The reference VSI measurements were conducted in [12].

The experiments with the presented identification results for the IPMSM in Fig. 6 (using ANN (19)), Fig. 7 (using ANN (19), (23)), and for the RSM in Fig. 8 (using ANN (18)), Fig. 9 (using ANN (18), (24)) as well as the VSI voltage error in Fig. 10 (using ANN (6)) highlight the capability of the proposed method to *simultaneously* identify

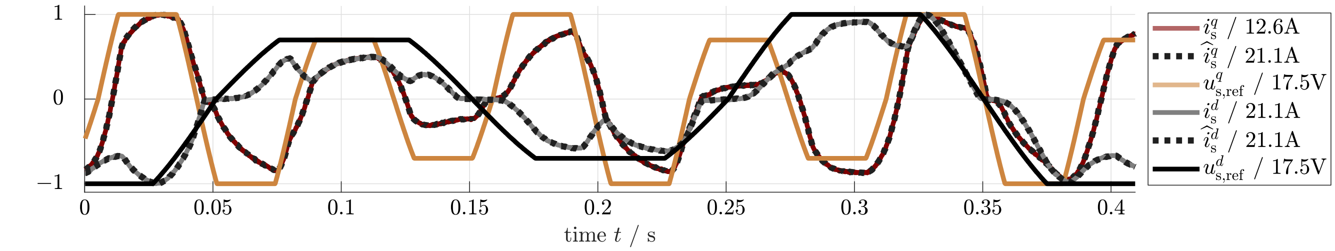

(a) Time series of the normalized stator d- and q-axis current and its estimate and stator voltage references.

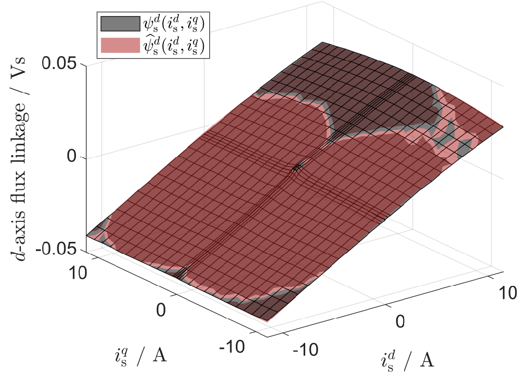

(b) Comparison of d-axis flux linkage $\psi_s^d(i_s^d, i_s^q)$ and its estimate $\widehat{\psi}_s^d(i_s^d, i_s^q)$.

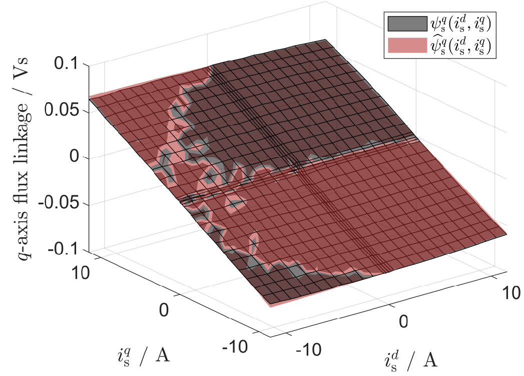

(c) Comparison of q-axis flux linkage $\psi_s^q(i_s^d, i_s^q)$ and its estimate $\widehat{\psi}_s^q(i_s^d, i_s^q)$.

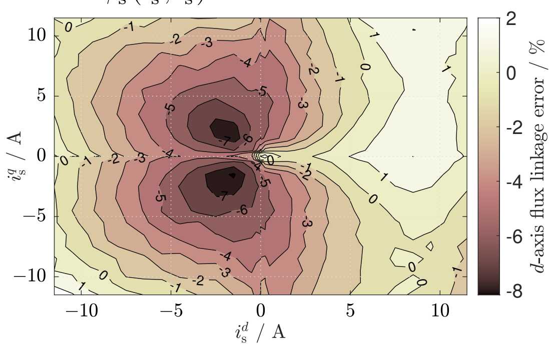

(d) Relative d-flux linkage error $\frac{\psi_s^d(i_s^d, i_s^q) - \widehat{\psi}_s^d(i_s^d, i_s^q)}{\psi_{s,\max}^d}$.

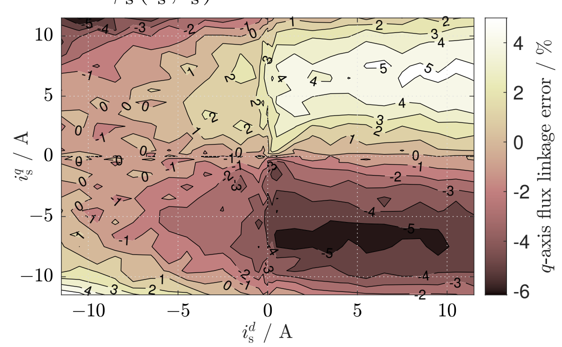

(e) Relative q-flux linkage error $\frac{\psi_s^q(i_s^d, i_s^q) - \widehat{\psi}_s^q(i_s^d, i_s^q)}{\psi_{s,\max}^q}$.

Figure 7: **IPMSM identification results:** (a) Time series; (b) & (c) flux linkage maps; (e) & (f) relative flux linkage errors.

(i) the VSI voltage deviations, (ii) the self-axis and cross-axis flux linkages and, therefore, the differential inductances as partial derivatives of the flux linkages as well and (iii) the phase resistance of IPMSM and RSM, respectively. The identification achieves high estimation accuracies compared to the actual VSI/machine nonlinearities and it is very fast as it takes a fraction of a second or a few seconds compared to DTMs with $\approx 45\,\text{min}$ or CSMs with $\approx 90\,\text{min}$ [9].

VI. Conclusion

In this paper, a simple and effective identification method for simultaneous estimation of voltage source inverter and electrical machine nonlinearities has been proposed and validated for an interior permanent magnet machine (IPMSM) and a synchronous reluctance machine (RSM). The estimation is based on structured artificial neural networks (ANNs). Experimental results have shown, that, at the same time, (i) the voltage deviations due to the VSI nonlinearities, (ii) the current-dependent self- and cross-axis flux linkages and differential inductances as well as (iii) the phase resistance can be estimated with good accuracy. The proposed identification concept is fast and does not require any a priori knowledge of the electrical drive in contrast to other available state-of-the-art methods, except for the rated current, voltage and frequency. Therefore, it can easily be applied in industrial applications (e.g. during end-of-line tests). Future work will focus on (i) other choices of ANN topologies and activation functions and (ii) online self-identification during normal operation; both in order to improve and refine the identification results further.

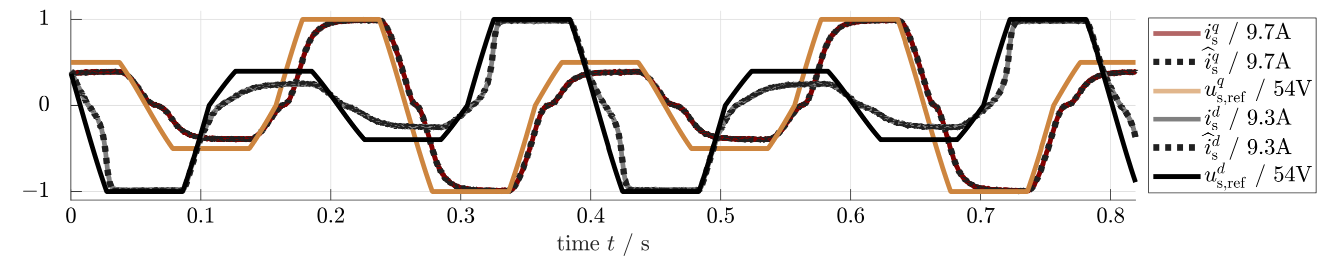

(a) Time series of the normalized stator d- and q-axis current and its estimate and stator voltage references.

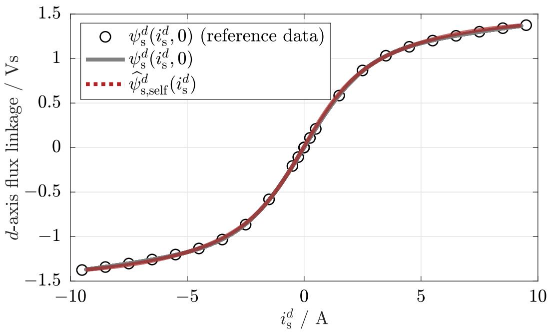

(b) Comparison of d-axis flux linkage $\psi_s^d(i_s^d, 0)$ and its self-axis estimate $\widehat{\psi}_{s,self}^d(i_s^d) = f_{ann}^{\psi,d}(i_s^d)$.

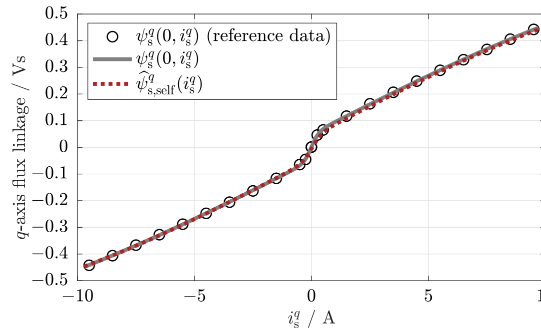

(c) Comparison of q-axis flux linkage $\psi_s^q(0, i_s^q)$ and its self-axis estimate $\widehat{\psi}_{s,self}^q(i_s^q) = f_{ann}^{\psi,q}(i_s^q)$.

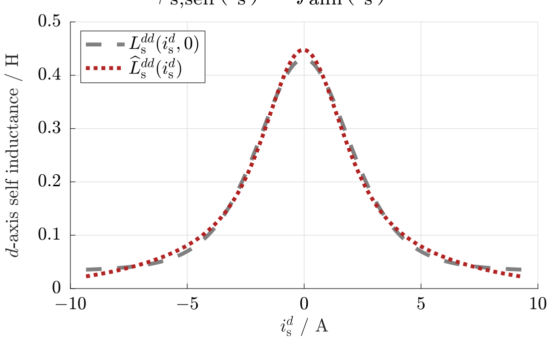

(d) Comparison of d-axis self inductance $L_s^{dd}(i_s^d, 0)$ and its estimate $\widehat{L}_s^{dd}(i_s^d) = \frac{\partial \widehat{\psi}_{s,self}^d(i_s^d)}{\partial i_s^d}$.

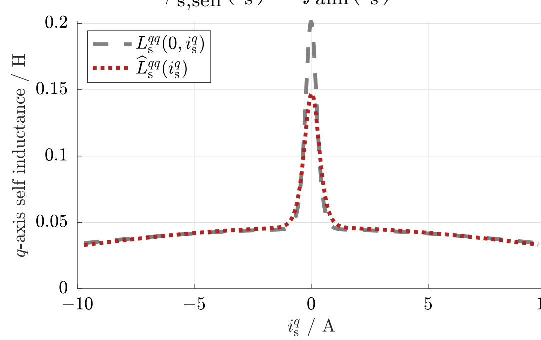

(e) Comparison of q-axis self inductance $L_s^{qq}(0, i_s^q)$ and its estimate $\widehat{L}_s^{qq}(i_s^q) = \frac{\partial \widehat{\psi}_{s,self}^q(i_s^q)}{\partial i_s^q}$.

Figure 8: **RSM identification results:** (a) Time series; (b) & (c) self-axis flux linkages; (d) & (e) differential inductances.

Acknowledgments

The authors would like to thank the Federal Ministry for "Economic Affairs and Climate Action" for their funding of this research (19I21030H - KIRA).

References

[1] S.A. Odhano, P. Pescetto, H.A.A. Awan, M. Hinkkanen, G. Pellegrino, and R. Bojoi. Parameter identification and self-commissioning in ac motor drives: A technology status review. *IEEE Transactions on Power Electronics*, 34(4):3603–3614, 2019.

[2] S. Wiedemann and R. Kennel. Self-Commissioning of the Current Control Loop in AC Drives. *International Exhibition and Conference for Power Electronics, Intelligent Motion, Renewable Energy and Energy Management, PCIM Europe*, 2018.

[3] Christoph M. Hackl, Maarten J. Kamper, Julian Kullick, and Joshua Mitchell. Current control of reluctance synchronous machines with online adjustment of the controller parameters. In *Proceedings of the 2016 IEEE International Symposium on Industrial Electronics (ISIE 2016)*, pages 153–160, Santa Clara, CA, USA, jun 2016. Institute of Electrical and Electronics Engineers (IEEE).

[4] H. Eldeeb, C. Hackl, L. Horlbeck, and J. Kullick. A unified theory for optimal feedforward torque control of anisotropic synchronous machines. *International Journal on Control, Taylor and Francis Group*, 2017.

[5] L. Ortombina, D. Pasqualotto, F. Tinazzi, and M. Zigliotto. Magnetic model identification of synchronous motors considering speed and load transients. *IEEE Transactions on Industry Applications*, 56(5):4945–4954, 2020.

[6] S. Wiedemann, S. Hall, R. Kennel, and M. Alaküla. Dynamic testing characterization of a synchronous reluctance machine. *IEEE Transactions on Industry Applications*, 54(2):1370–1378, 2018.

[7] G. Pellegrino, B. Boazzo, and T. M. Jahns. Magnetic Model Self-Identification for PM Synchronous Machine Drives. *IEEE Transactions on Industry Applications*, 51(3):2246–2254, May 2015.

[8] P. Pescetto and G. Pellegrino. Sensorless magnetic model and pm flux identification of synchronous drives at standstill. *IEEE International Symposium on Sensorless Control for Electrical Drives (SLED)*, 2017.

[9] S. Wiedemann. *Self-Identification and Automatic Tuning of Synchronous Machine Drives*. PhD thesis, Technical University of Munich, 2020.

[10] M. Van Werkhoven and R. Brunner. C.U. 4E EMSA Policy guidelines for motor driven units - Pumps, fans and compressors. *10th International Conference on Energy Efficiency in Motor Driven System (EEMODS), Rome, Italy*, 2017.

[11] I. Bojoi, E. Armando, G. Pellegrino, and S. G. Rosu. Self-commissioning

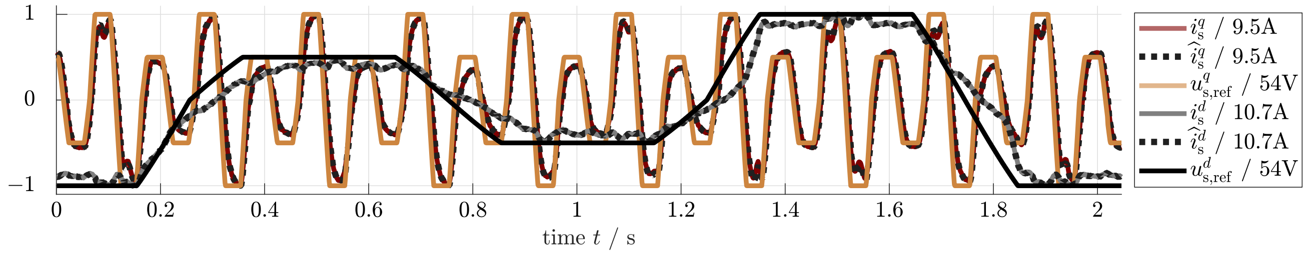

(a) Time series of the normalized stator d- and q-axis current and its estimate and stator voltage references.

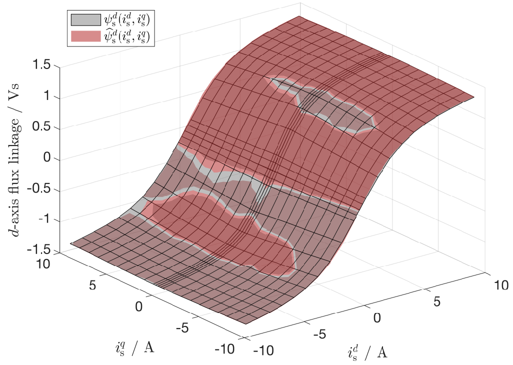

(b) Comparison of d-axis flux linkage $\psi_s^d(i_s^d, i_s^q)$ and its estimate $\widehat{\psi}_s^d(i_s^d, i_s^q)$.

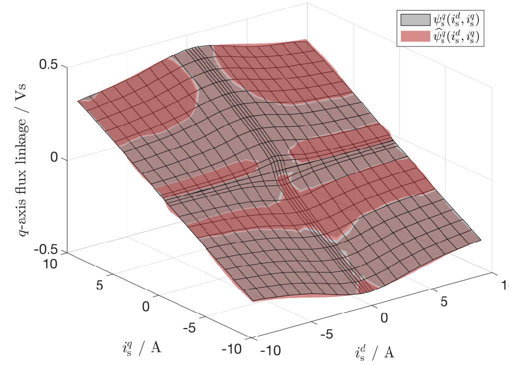

(c) Comparison of q-axis flux linkage $\psi_s^q(i_s^d, i_s^q)$ and its estimate $\widehat{\psi}_s^q(i_s^d, i_s^q)$.

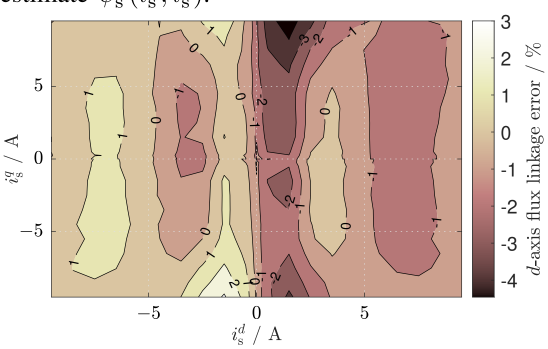

(d) Relative d-flux linkage error $\frac{\psi_s^d(i_s^d,i_s^q)-\widehat{\psi}_s^d(i_s^d,i_s^q)}{\psi_{s,\max}^d}$.

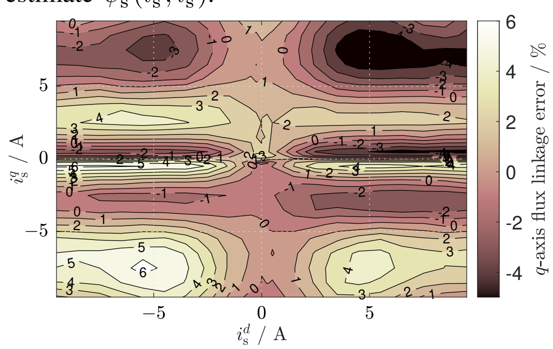

(e) Relative q-flux linkage error $\frac{\psi_s^q(i_s^d,i_s^q)-\widehat{\psi}_s^q(i_s^d,i_s^q)}{\psi_{s,\max}^q}$.

Figure 9: **RSM identification results:** (a) Time series; (b) & (c) flux linkages; (e) & (f) relative flux linkage errors.

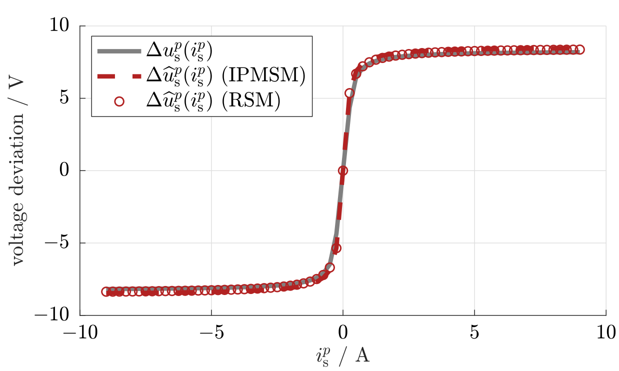

Figure 10: **IPMSM and RSM identification results:** Comparison of VSI voltage deviations $\Delta u_s^p(i_s^p)$ and their estimates $\Delta\widehat{u}_s^p(i_s^p)$ (d and q axis give very similar results).

of inverter nonlinear effects in AC drives. *IEEE International Energy Conference and Exhibition (ENERGYCON)*, pages 213–218, Sept 2012.

[12] S. Wiedemann and R. Kennel. Accurate Self-Identification of Inverter Nonlinear Effects in AC Drives. *International Exhibition and Conference for Power Electronics, Intelligent Motion, Renewable Energy and Energy Management, PCIM Europe*, 2018.

[13] D. Salt, D. Drury, D. Holliday, A. Griffo, P. Sangha, and A. Dinu. Compensation of Inverter Nonlinear Distortion Effects for Signal-Injection-Based Sensorless Control. *IEEE Transactions on Industry Applications*, 47(5), 2011.

[14] L. Ortombina, F. Tinazzi, and M. Zigliotto. Magnetic Modelling of Synchronous Reluctance and Internal Permanent Magnet Motors Using Radial Basis Function Networks. *IEEE Transactions on Industrial Electronics*, 2017.

[15] S. Wiedemann and R. Kennel. Encoderless Self-Commissioning and Identification of Synchronous Reluctance Machines at Standstill. *IEEE 26th International Symposium on Industrial Electronics (ISIE)*, June 2017.

[16] N. Bedetti, S. Calligaro, and R. Petrella. Stand-Still Self-Identification of Flux Characteristics for Synchronous Reluctance Machines Using Novel Saturation Approximating Function and Multiple Linear Regression. *IEEE Transactions on Industry Applications*, 52(4):3083–3092, 2016.

Table III: IPMSM and RSM identification results including the phase resistance R_s (obtained from [41] Sec. 5, [9]), its estimate $\widehat{R}_\mathrm{s}$ & relative error in % ($b_2^{d,\mathrm{self}}$ obtained from [6]).

	IPMSM		**RSM**	
	d-**axis**	q-**axis**	d-**axis**	q-**axis**
R_s	$0.45\,\Omega$	$0.45\,\Omega$	$4.72\,\Omega$	$4.72\,\Omega$
$\widehat{R}_\mathrm{s}^x$; $\frac{\widehat{R}_\mathrm{s}^x - R_\mathrm{s}}{R_\mathrm{s}}$	0.49Ω; 9%	0.48Ω; 6%	4.68Ω; 1%	4.64Ω; 2%
$w_{1,1}^{\mathrm{vsi}}$	7.658	6.488	-6.675	8.142
$w_{1,2}^{\mathrm{vsi}}$	11.54	10.62	-7.386	3.957
$b_{1,1}^{\mathrm{vsi}}$	0.4859	0.2905	0.8266	-0.1667
$w_{2,1}^{\mathrm{vsi}}$	5.993	6.426	-4.613	6.447
$w_{2,2}^{\mathrm{vsi}}$	2.583	2.084	-3.883	1.881
$b_{1,2}^{\mathrm{vsi}}$	-2.115	-2.151	-3.245	7.824
$w_{1,1}^{x,\mathrm{self}}$	–	–	0.4849	0.06072
$w_{1,2}^{x,\mathrm{self}}$	–	–	-0.1625	2.345
$b_{1,1}^{x,\mathrm{self}}$	–	–	0.01482	-0.003926
$w_{2,1}^{x,\mathrm{self}}$	0.003554	0.005608	0.6599	0.7583
$w_{2,2}^{x,\mathrm{self}}$	0.0005852	0	-0.7862	0.04309
$b_{1,2}^{x,\mathrm{self}}$	–	–	-0.00678	-0.0544
$b_{2}^{x,\mathrm{self}}$	0.0685	–	–	–
$w_{2,1}^{x,\mathrm{cross}}$	0.038796		-0.210865	
$w_{2,2}^{x,\mathrm{cross}}$	0.036888		-19.663191	
$w_{2,3}^{x,\mathrm{cross}}$	0.002055		–	
$w_{1,1,1/1,1}^{x,\mathrm{cross}}$	-0.005107	-0.007110	0.356393	-0.266645
$w_{1,1,2}^{x,\mathrm{cross}}$	0.008513	-0.000375	–	–
$w_{1,1,3}^{x,\mathrm{cross}}$	0.006492	0.002031	–	–
$w_{1,2,1/1,2}^{x,\mathrm{cross}}$	0.013578	0.001272	-0.155646	0.018622
$w_{1,2,2}^{x,\mathrm{cross}}$	0.000498	-0.048376	–	–
$w_{1,2,3}^{x,\mathrm{cross}}$	-0.005737	-0.004789	–	–
$w_{1,3,1}^{x,\mathrm{cross}}$	0.006845	0.006610	–	–
$w_{1,3,2}^{x,\mathrm{cross}}$	0.002189	0.002987	–	–
$w_{1,3,3}^{x,\mathrm{cross}}$	0.024363	-0.019914	–	–
$b_{1,1}^{x,\mathrm{cross}}$	0.006003	0.028532	–	–
$b_{1,2}^{x,\mathrm{cross}}$	0.000243	0.002877	–	–
$b_{1,3}^{x,\mathrm{cross}}$	0.003881	0.006408	–	–

[17] Shih-Wei Su, Christoph Michael Hackl, and Ralph Kennel. Analytical prototype functions for flux linkage approximation in synchronous machines. *IEEE Open Journal of the Industrial Electronics Society*, pages 1–1, 2022.

[18] Z. Qu, T. Tuovinen, and M. Hinkkanen. Inclusion of magnetic saturation in dynamic models of synchronous reluctance motors. *International Conference on Electrical Machines*, pages 994–1000, 2012.

[19] M. Seilmeier and B. Piepenbreier. Identification of steady-state inductances of PMSM using polynomial representations of the flux surfaces. *39th Annual Conference of the IEEE Industrial Electronics Society (IECON)*, pages 2899–2904, 2013.

[20] S. Kuehl, P. Landsmann, and R. Kennel. Bivariate polynomial approximation of cross-saturated flux curves in synchronous machine models. *IEEE International Energy Conference and Exhibition (ENERGYCON)*, pages 219–224, Sept. 2012.

[21] E. Armando, R. Bojoi, P. Guglielmi, G. Pellegrino, and M. Pastorelli. Experimental Identification of the Magnetic Model of Synchronous Machines. *IEEE Transactions on Industry Applications*, 49(5):2116–2125, Sept. 2013.

[22] A. Varatharajan, G. Pellegrino, and E. Armando. Kinetic-rotor self-commissioning of synchronous machines for magnetic model identification with online adaptation. *IEEE Transactions on Industry Applications*, pages 1–1, 2022.

[23] M. Hinkkanen, P. Pescetto, E. Molsa, S. Saarakkala, G. Pellegrino, and R. Bojoi. Sensorless self-commissioning of synchronous reluctance motors at standstill without rotor locking. *IEEE Transactions on Industry Applications*, 2016.

[24] Paolo Pescetto and Gianmario Pellegrino. Sensorless standstill commissioning of synchronous reluctance machines with automatic tuning. In *2017 IEEE International Electric Machines and Drives Conference (IEMDC)*, pages 1–8, 2017.

[25] Y. Murai, T. Watanabe, and H. Iwasaki. Waveform Distortion and Correction Circuit for PWM Inverters with Switching Lag-Times. *IEEE Transactions on Industry Applications*, pages 881–886, September 1987.

[26] Y. Murai, A. Riyanto, H. Nakamura, and K. Matsui. PWM strategy for high frequency carrier inverters eliminating current clamps during switching dead-time. *Conference Record of the 1992 IEEE Industry Applications Society Annual Meeting*, pages 317–322, October 1992.

[27] J. Holtz and J. Quan. Sensorless vector control of induction motors at very low speed using a nonlinear inverter model and parameter identification. *Conference Record of the 2001 IEEE Industry Applications Conference. 36th IAS Annual Meeting*, pages 2614–2621, September 2001.

[28] N. Pothi, S. Premrudeepreechacharn, and C. Rakpenthai. Voltage Losses Compensation Using Artificial Neural Network for Estimation Nonlinear Characteristic of Switches. *International Conference on Power Electronics and Drive Systems*, pages 1015–1019, November 2007.

[29] A. R. Munoz and T. Lipo. On-line dead-time compensation technique for open-loop PWM-VSI drives. *IEEE Transactions on Power Electronics*, 14(4):683–689, July 1998.

[30] Y. Park and S. Sul. A novel method utilizing trapezoidal voltage to compensate for inverter nonlinearity. *IEEE Transactions on Power Electronics*, 27(12):4837–4846, 2012.

[31] Max A. Buettner, Niklas Monzen, and Christoph M. Hackl. Artificial neural network based optimal feedforward torque control of interior permanent magnet synchronous machines: A feasibility study and comparison with the state-of-the-art. *Energies*, 15(5):1838, 2022.

[32] S. Wiedemann and R. Kennel. Modelling of Inverter Nonlinear Effects. *International Exhibition and Conference for Power Electronics, Intelligent Motion, Renewable Energy and Energy Management, PCIM Europe*, 2018.

[33] Christoph M. Hackl. *Non-identifier based adaptive control in mechatronics: Theory and Application*. Number 466 in Lecture Notes in Control and Information Sciences. Springer International Publishing, Berlin, 2017.

[34] Shih-Wei Su, Christoph M. Hackl, and Ralph Kennel. Analytical prototype functions for flux linkage approximation in synchronous machines. *IEEE Open Journal of the Industrial Electronics Society*, 3:265–282, 2022.

[35] Xavier Glorot, Antoine Bordes, and Y. Bengio. Deep sparse rectifier neural networks. *International Conference on Artificial Intelligence and Statistics (AISTAT)*, 14, 2011.

[36] Hisham Eldeeb, Christoph M. Hackl, Lorenz Horlbeck, and Julian Kullick. A unified theory for optimal feedforward torque control of anisotropic synchronous machines. *International Journal of Control*, 2017.

[37] Dierk Schröder and Martin Buss. *Intelligente Verfahren: Identifikation und Regelung nichtlinearer Systeme*. Springer-Verlag, Berlin, 2017.

[38] S.A. Odhano, P. Giangrande, R. Bojoi, and C. Gerada. Self-commissioning of interior permanent magnet synchronous motor drives with high-frequency current injection. In *2013 IEEE Energy Conversion Congress and Exposition*, pages 3852–3859, 2013.

[39] Lennart Ljung. *System Identification*. Prentice Hall PTR, 2 edition, 1999.

[40] E. Howard, M. Kamper, and S. Gerber. Asymmetric flux barrier and skew design optimization of reluctance synchronous machines. *IEEE Transactions on Industry Applications*, 51(5):3751–3760, 2015.

[41] PMSM Electrical Parameters Measurement. Application note, number: an4680, rev. 0, 02/2013, Freescale Semiconductor, Feb. 2013.

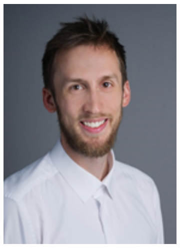

SIMON WIEDEMANN was born in Kassel, Germany, in 1987. He received the B.Eng. degree in electrical engineering and information technology from the Hamburg University of Applied Sciences, Hamburg, Germany, in 2012, the M.Sc. degree in Electrical Power from the University of Newcastle-Upon-Tyne, Newcastle-Upon-Tyne, U.K., in 2014 and his Dr.-Ing. (Ph.D.) degree in the Institute for Electrical Drive Systems and Power Electronics, Technical University of Munich, Munich, Germany, as a Marie Curie Research Scholar in 2021. Since 2014 he is with the Research and Development Department, MACCON GmbH, Munich, Germany. His research interests include self-commissioning, characterisation and control of electrical drives.

CHRISTOPH M. HACKL (M'12-SM'16) was born in 1977 in Mannheim, Germany. After studying Electrical Engineering (with focus on mechatronics and systems and control) at Technical University of Munich (TUM), Germany and University of Wisconsin-Madison, USA, he received the B.Sc., Dipl.-Ing., and Dr.-Ing. (Ph.D.) degrees in Electrical Engineering in 2003, 2004 and 2012, respectively, from TUM. Since 2004, he has been teaching electrical drives, power electronics, and mechatronic & renewable energy systems. Since 2014, he has been the head of the research group "Control of Renewable Energy Systems (CRES)" at TUM. In 2018, he became a Professor for Electrical Machines and Drives and the head of the "Laboratory for Mechatronic and Renewable Energy Systems (LMRES)" at the Hochschule München (HM) University of Applied Sciences, Germany. In 2019, he completed his habilitation on "Mechatronic and Renewable Energy Systems" and co-founded the research Institute for Sustainable Energy Systems (ISES) at HM, which he co-heads since then. His research interests include nonlinear, adaptive and optimal control and design of electrical drives, and mechatronic and renewable energy systems.